

# 1 Glacial-interglacial shifts in dominant climate forcing over the last 33 2 ka in the northern South China Sea

3 Xueqin Zhao<sup>\*1</sup>, Shengjie Ye<sup>1</sup>, Jiahui Yao<sup>1</sup>, Michael E. Meadows<sup>2,3</sup>, Chengyu Weng<sup>4</sup>, Yasong Wang<sup>1</sup>,  
4 Mingxing Zhang<sup>1</sup>, Yunping Xu<sup>1</sup>

5 <sup>1</sup>Shanghai Frontiers Research Center of the Hadal Biosphere, College of Oceanography and Ecological Science, Shanghai  
6 Ocean University, Shanghai 201306, China

7 <sup>2</sup>School of Geography and Ocean Sciences, Nanjing University, Nanjing 210023, China

8 <sup>3</sup>Department of Environmental & Geographical Science, University of Cape Town, Cape Town 7701, South Africa

9 <sup>4</sup>State Key Laboratory of Marine Geology, Tongji University, Shanghai, China

10 *Correspondence to:* Xueqin Zhao (xqzhao@shou.edu.cn)

11 **Abstract.** The northern South China Sea (SCS) is a critical region for understanding East Asian Monsoon dynamics. However,  
12 integrated, multi-proxy records elucidating long-term climatic and vegetation changes in this region remain fragmented, with  
13 a notable scarcity of coherent land-ocean interaction data during the Last Glacial Maximum (LGM). This gap has impeded  
14 progress in elucidating the mechanisms underpinning monsoon variability and in rigorously evaluating the performance of  
15 palaeoclimate models. To address this, we conducted a multi-proxy analysis combining palynological, organic- and inorganic-  
16 geochemical methods on a marine sediment core from the northern South China Sea to reconstruct environmental and oceanic  
17 dynamics at millennial-scale resolution that spans the last 33 ka. Our results reveal a clear contrast between glacial and  
18 interglacial conditions and drivers/regimes. The glacial period, especially the LGM, was characterized by higher  
19 sedimentation rates, elevated marine primary productivity, cooler climate, lower humidity and drier conditions, herb-  
20 dominated vegetation, associated with enhanced and intensified fire activity in the adjacent terrestrial ecosystems. This regime  
21 was dominantly forced by low sea level and glacial aridity, which together promoted open terrestrial vegetation and enhanced  
22 nutrient input to the ocean. The deglaciation was characterized by pronounced warming, and reduced productivity, together  
23 with increased moisture availability, a shift toward pine-dominated vegetation, and minimal reduced fire activity, and reduced  
24 fluvial input as the coastline retreated. A key finding is the ocean warming which began around 1.3 ka earlier than major  
25 terrestrial changes, indicating that tropical ocean-atmosphere interactions initiated the deglacial transition. The overall findings  
26 highlight a fundamental transition in climatic controls, from a glacial regime dominated by sea-level-driven shelf exposure  
27 and arid climate dominated by sea level forcing during the glacial period to one increasingly an interglacial regime governed  
28 by tropical ocean-atmosphere interactions initiated by early ocean warming during the interglacial dynamics. This study  
29 underscores the sensitivity of the northern SCS to both high- and low-latitude forcing and the value of integrated land-sea  
30 proxies in deciphering complex climate interactions.

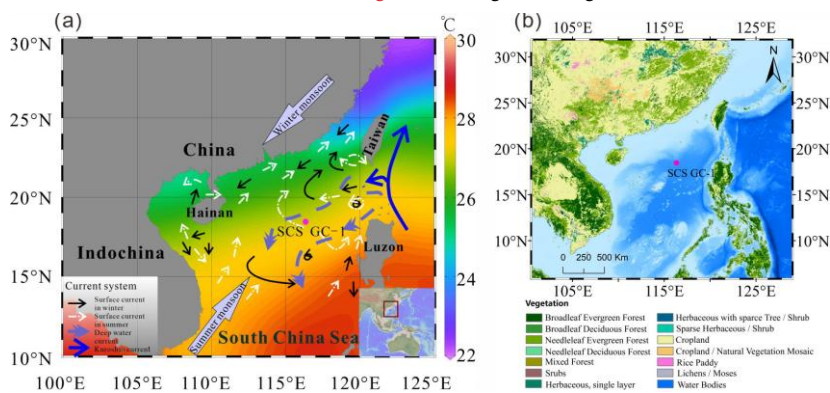
## 31 1 Introduction

32 Low latitude regions play a critical role in the global climate and its dynamic because they are the seat of the most active  
33 moisture and heat exchanges between the atmosphere and the ocean expressed via the monsoon regime. Tropical and  
34 subtropical monsoon regions such as East Asia and the South China Sea (SCS) experience the most significant seasonal  
35 reversal in wind directions with associated migration of regional intense precipitation (Wang et al., 2017). Monsoon wind and  
36 precipitation patterns have changed significantly in the late Quaternary, influenced by gradual changes in insolation and  
37 internal interactions among the atmosphere, oceans, land surfaces and Northern Hemisphere ice sheets (An, 2000; Ding et al.,  
38 1994; Kissel et al., 2020; Tian et al., 2010; Wang et al., 2001). These changes have affected the climate and land-ocean energy  
39 balance of western Pacific marginal basins, whereas the influence and dynamics of the monsoon system remain insufficiently  
40 constrained. Investigations of palaeoclimate variability have significant value in providing valuable insights into monsoonal  
41 dynamics across tectonic, orbital and millennial time scales.

Formatted: Font: (Asian)+Body Asian (宋体), (Asian) Chinese (Simplified, Mainland China)

42 Given the importance of the climate signature during the last Glacial Maximum (LGM, spanning approximately 26.5-19 ka)  
 43 to climate model validation and testing, new reconstructions of precipitation and vegetation response during the LGM are  
 44 necessary to resolve inconsistencies and improve model reliability. Marine sediments potentially record the interplay of the  
 45 East Asian Monsoon, surface and deep oceanic circulation and sea level compared with other terrestrial records (Tian et al.,  
 46 2004; Wang et al., 1999). The South China Sea is divided into a northern deep basin with isolated, oxygen-poor waters and a  
 47 southern extensive shelf province, a dichotomy fundamentally controlled by a ~2400 m deep sill that restricts deep-water  
 48 exchange with the open Pacific (Chen and Huang, 1996). Due to its well-preserved sedimentary strata, abundant sediment  
 49 supply, and relatively high sedimentation rates, the northern SCS is recognized as a key area with strong potential for high-  
 50 resolution palaeoenvironmental reconstructions. Such records can substantially enhance our ability to resolve global and  
 51 regional climate variability during the Quaternary (Wang et al., 2014). A range of different proxies is preserved in marine  
 52 sedimentary archives. Pollen evidence, for example, can provide a valuable signal of vegetation evolution on the adjacent  
 53 continental land mass (Cheng et al., 2023; Luo et al., 2016; Sun et al., 2000a), while microcharcoal particles are widely used  
 54 in palaeofire reconstruction to infer fire frequency, intensity and vegetation changes, and terrestrial ecosystem response  
 55 (Conedera et al., 2009). Foraminifera are sensitive to environmental changes, and are widely applied as a palaeo-proxy of  
 56 marine conditions (Haynes, 1981), although the shells of planktonic foraminifera are susceptible to dissolution which may  
 57 have limitations. Organic walled dinoflagellate cysts (dinocysts), the resting cysts formed during the sexual reproduction  
 58 process of these taxa, are characterized by resistant organic matter and are also generally well preserved in marine sediments  
 59 (Dale, 1996; Zonneveld et al., 2013). The well-known correlation of modern dinocyst distribution with distinct physical marine  
 60 water properties such as sea surface temperature (SST), salinity, nutrients and productivity indicates the value of dinocysts as  
 61 a proxy in palaeoceanographic reconstruction, although current research on dinocysts in the South China Sea remains largely  
 62 confined to their modern distribution in marine surface sediments (Li et al., 2018a; Li et al., 2020; Li et al., 2023). Fossil  
 63 dinocyst records in the SCS are scarce (Li et al., 2021; Li et al., 2017).

64 While previous studies have documented glacial-interglacial changes in vegetation and oceanography in the northern SCS, the  
 65 relative importance of different forcing mechanisms-particularly the high- and low-latitude forcing across these transitions  
 66 remain uncertain. Given the complementary strengths of different archives To address this, we adopt a multi-proxy approach  
 67 in this study, combining palynological indicators (pollen, spores, microcharcoal, and dinocysts), organic geochemical proxies  
 68 (TOC and TN), and inorganic geochemical markers (element ratios,  $\delta^{13}\text{C}$  and  $\delta^{18}\text{O}$ , and Mg/Ca-based SST of planktonic  
 69 foraminifera) to reconstruct vegetation, fire regimes, sediment sources, ocean productivity, and sea surface temperature. A  
 70 marine sediment core (SCS-GC-1; Fig. 1a) recovered from the northern SCS was analyzed to reconstruct millennial-scale  
 71 climate and ocean dynamics over the last 33 ka. The specific aims of this study are: (1) to reconstruct the palaeovegetation and  
 72 palaeoclimate; (2) to document the evolution of palaeoceanographic conditions; and (3) to clarify the mechanisms governing  
 73 how land-ocean interactions and dominant climate forcings shift across glacial-interglacial transitions.



74

75 **Figure 1:** (a) Map of the East Asian monsoon system and ocean circulations with annual modern mean annual sea surface  
76 temperature (Data from World Ocean Atlas, 2023) and the location of core SCS GC-1 (red) retrieved from the northern SCS.  
77 (b) Map of the distribution of vegetation types in the main areas around the South China Sea retrieved from Stibig et al. (2007)  
78 and <https://forobs.jrc.ec.europa.eu/products/glc2000/products.php>. The black solid line indicates the position of the winter  
79 surface current, the white dashed line is the position of the summer surface current, the purple dashed line is the deep current,  
80 and the blue solid line is the Kuroshio Current.

## 81 2 Environmental setting

### 82 2.1 Atmospheric circulation and climate

83 The northern SCS experiences a subtropical to tropical climate with high temperatures (15-28°C annually): the mean air  
84 temperatures range from 15-25°C during the coldest month (January), and ~28°C during the warmest month (July). Rainfall  
85 is copious with an annual mean of 1000-2000 mm (Li et al., 2017). ~~that~~The climate is primarily governed by the seasonal East  
86 Asian Monsoon system: northeasterly winds prevail during winter (December-February) and southwesterlies dominate in  
87 summer (June-August) (Chao et al., 1995; Wang et al., 2017). In winter, decreasing temperatures over the Asian continent lead  
88 to the development and intensification of a cold high-pressure system over Inner Mongolia, while the Aleutian Low strengthens  
89 over the North Pacific. The resulting continent-ocean pressure gradient drives the East Asian Winter Monsoon (EAWM),  
90 transporting cold, dry northeasterly air masses southwards across China into the SCS. In summer, this pattern reverses: the  
91 continental system is replaced by the Indian Low, and stronger high-pressure systems develop over the North Pacific and the  
92 Australian region, generating the East Asian Summer Monsoon (EASM), which advects warm, moist-laden air from the ocean  
93 onto the Chinese mainland (Liu et al., 2016a).

### 94 2.2 Oceanic circulation

95 Surface currents in the SCS are controlled by seasonal variations in the dominant wind directions related to the EASM and  
96 EAWM (Hu et al., 2000), monsoon-topography interactions, and additional influences from wind-stressed eddies. During  
97 winter, the EAWM drives a strong southward western boundary current along the Vietnamese and southern Chinese coasts,  
98 associated with a basin-scale cyclonic circulation. In contrast, summer circulation is weaker and more complex, with coastal  
99 currents generally reversing to flow northward under EASM influence.

100 The EASM drives distinct northern and southern circulation patterns in the SCS, which form two anticyclonic eddies separated  
101 near 12°N by a strong upwelling off Vietnam (Fang et al., 1998). In addition, the region is influenced by the intrusion of warm,  
102 saline Kuroshio waters entering through the Luzon strait between Luzon from Taiwan (Huang et al., 2025).

103 Seasonal variations in marine primary productivity are primarily modulated by the East Asian Monsoon (Liu et al., 2002).  
104 During winter, stronger northeasterlies induce eutrophic conditions in the upper euphotic layer, elevating marine primary  
105 productivity. In summer, persistent heating of warmer, lower-density surface waters intensifies stratification, leading to  
106 oligotrophic conditions and reduced primary productivity (Liu et al., 2002; Zhang et al., 2016).

### 107 2.3 Vegetation

108 Vegetation types on the adjacent continental landmass around the SCS are diverse and reflect regional climate conditions (Luo  
109 and Sun, 2013), although they are dominated by tropical and subtropical broadleaved evergreen forests (Fig. 1b) (Stibig et al.,  
110 2007). Whereas tropical rain forest vegetation, characterized by taxa such as Dipterocarpaceae, Moraceae, Sapindaceae and  
111 Sapotaceae, occurs at low altitudes on tropical islands along the southern coast of the Chinese mainland, e.g., Hainan Island,  
112 and southern Taiwan Island, Ttropical monsoon forests are distributed widely throughout the Indochina Peninsula and along  
113 the coast of southeastern China with the representative species including Verbenaceae, Dipterocarpaceae, as well as pine trees  
114 (including *Pinus merkusii*, *Pinus kesiya*, and *Pinus insularis*) which are dominant in the composition of monsoon mountain  
115 forest.a. Subtropical evergreen forests, mainly composed of the families Fagaceae (e.g., *Cyclobalanopsis* and *Quercus*),

Formatted: Not Highlight

Formatted: Not Highlight

Formatted: Not Highlight

Formatted: Not Highlight

Formatted: Font: Italic

Formatted: Font: Italic

Formatted: Font: Italic

Formatted: Not Highlight

Formatted: Font: Italic

Formatted: Not Highlight

Formatted: Font: Italic, Not Highlight

116 **Lauraceae, and Theaceae, Hamamelidaceae and Magnoliaceae** are prominent between 24°N and 25°N on southeast-facing  
117 hills and on high plateaus (Wang, 1961; Whitmore, 1985). Generally, the abundance of both tropical and subtropical taxa  
118 increase gradually towards the south in eastern China, indicating the significance of the north-south temperature gradient (Dai  
119 and Weng, 2015; Dai et al., 2015). The vegetation types occurring in southeast and southern China, as well as Taiwan Island,  
120 are the main pollen sources of the northern SCS (Dai and Weng, 2011; Sun et al., 1999).

## 121 2.4 Sedimentation rates

122 The SCS receives enormous amounts of terrigenous sediments (ca.  $700 \times 10^6$  tons/year) every year, mainly during the rainy  
123 season in summer. The sediments originate from the erosion/weathering of rocks in the catchment basins particularly from  
124 three Asian rivers (the Red River, the Pearl River, and the Mekong River) which are among the largest in the world (Liu et al.,  
125 2010; Milliman and Syvitski, 1992). Beyond the river deltas, part of the terrigenous sediments is deposited on the shelves  
126 (Zhong et al., 2017), while the rest reaches the open sea where the sediment is transported by the oceanic currents and deposited  
127 on the continental slope and in the deep basins (Liu et al., 2013).

## 128 3. Materials and methods

### 129 3.1 Materials and chronological analysis

130 The 305 cm long marine sediment core SCS GC-1 was retrieved from the northern SCS during R/V Songhang (Shanghai  
131 Ocean University) cruise in October 2022 (18.47°N, 116.34°E; water depth of 3764 m) (Fig. 1).

132 Eight accelerator mass spectrometry AMS  $^{14}\text{C}$  dates at depths of 20 cm, 45 cm, 65 cm, 90 cm, 107 cm, 133 cm, 203 cm and  
133 275 cm were obtained on mixed planktic foraminiferal (including *Globigerinoides ruber*, *Globigerinoides sacculifer*,  
134 *Neogloboquadrina dutertrei*, *Pulleniatina obliquiloculata*, *Orbulina universa*) tests isolated from the core. AMS  $^{14}\text{C}$   
135 measurements were carried out on a NEC 0.5Mev  $^{14}\text{C}$  AMS (National Electrostatics Corporation, NEC) at Guangzhou Institute  
136 of Geochemistry, Chinese Academy of Sciences (GIGCAS).

### 137 3.2 X-ray fluorescence (XRF) analysis

138 The core was non-destructively scanned using the Avaatech XRF Core Scanner at the State Key Laboratory of Marine Geology,  
139 Tongji University. The parameters of the Avaatech XRF core scanner were set for 30 s exposure time, three voltage and current  
140 conditions with 10 kv and 0.75 mA for Al-Fe, 30 kV and 0.5 mA for Co-Mo, and 50 kV and 0.2 mA for Tc-U. The scanning  
141 area was 5 mm (length)  $\times$  10 mm (width), and at a scanning time of 30 s. The relative content of each element including Al to  
142 Ba which was obtained, is expressed in cps as counts per second.

### 143 3.3 TOC and TN analysis

144 Approximately 1 g of each freeze-dried sample was treated with diluted 3 mol/L HCl for 24 hours at room temperature to  
145 remove inorganic carbonates. After the reaction, the samples were repeatedly rinsed with ultrapure water ( $\geq 18 \text{ M}\Omega \cdot \text{cm}$ ) and  
146 centrifuged until the supernatant reached a neutral pH. The remaining residue was oven-dried at 60°C, ground and then  
147 weighed. The decarbonated samples were analyzed for elemental content using a Vario EL cube elemental analyzer (Elementar,  
148 Germany) at the State Key Laboratory of Marine Geology, Tongji University, employing the dry combustion method.  
149 Replicate analyses were conducted to ensure data reliability, with average standard deviations of  $\leq 0.1 \text{ wt}\%$  for both TOC and  
150 TN measurements.

### 151 3.4 Planktonic foraminiferal isotopic and Mg/Ca analysis

152 The samples were freeze-dried, disaggregated by soaking in water for 1-2 days, then were rinsed repeatedly through a 63 µm  
153 sieve to remove organic matter and fine impurities. The rinsed wet samples were then dried at 60°C (approximately 24 h) and  
154 passed through a 125 µm and 250 µm sieve, respectively (Schönfeld et al., 2012). *G. ruber* larger than 250 µm size were  
155 selected under a microscope. For each sample, clean and intact *G. ruber* (around 30 specimens) were picked and tested using  
156 a Finnigan MAT253 Mass Spectrometer. The δ<sup>18</sup>O results are reported versus VPDB after calibration with NBS 19. The  
157 average test accuracy is ±0.07%.

158 For the Mg/Ca analysis, surface dwelling foraminiferal species with smooth-surface individuals of *G. ruber* between 250-350  
159 µm (ca. 0.3 mg) were picked to ensure no obvious contamination or damage, and that the atrioventricular structure was intact  
160 (Barker et al., 2003). The analysis was performed on a quadrupole inductively coupled plasma mass spectrometry (ICP-MS).  
161 Duplicate measurements of two samples yield an average relative deviation of 0.064 mmol/mol, confirming that analytical  
162 uncertainty is minimal and does not materially affect interpretation. Sea surface temperatures were reconstructed following  
163 Eq. (1) (Huang et al., 2008):

$$164 SST=0.5*(\ln(Mg/Ca/0.3)/0.09+\ln(Mg/Ca/(0.38-0.02*D)))/0.09 \quad (1)$$

165 Where *SST* represents mean annual sea surface temperature (°C), *Mg/Ca* is the *G. ruber* based Mg/Ca ratio (mmol/mol), *D* is  
166 water depth of the core (km).

### 167 3.5 Palynological analysis

168 In total, 61 samples (mean interval 4 cm) were processed for palynological analysis at Shanghai Ocean University following  
169 standard preparation procedures. Samples were treated sequentially with 10% HCl, 40% HF, 30% HCl, sieved with 125 µm  
170 and 7 µm meshes, and mounted for microscopic examination. Routine identification was performed under a [light microscope](#)  
171 [\(ZEISS Promostar 3\)](#) ~~microscope~~ at 400x magnification, with 1000x used for detailed taxonomic identification. Four  
172 *Lycopodium* spore tablets with 10315±845 spores were added to each sample prior to processing to enable calculation of pollen  
173 concentration. Pollen taxa were identified using the reference of Tang et al. (2020). At least 300 pollen grains (including  
174 terrestrial pollen taxa, sedges and aquatic taxa) were counted for most of the samples. The percentages of pollen taxa were  
175 calculated based on the pollen sum ~~excluding *Pinus*~~, and the percentages of spore taxa were calculated based on pollen and  
176 spore sum. ~~The 95% confidence intervals of percentages were calculated following Maher (1972).~~

177 Charcoal particles were identified and counted on the same microscope slides prepared for pollen analysis. Only particles  
178 which were black, opaque and angular were considered as charcoal. Particles smaller than 10 µm were not counted due to the  
179 risk of false identification (Mooney and Tinner, 2011). More than 1500 charcoal particles (with an average of 3500 particles)  
180 were counted for each sample. Two size classes were defined, based on the length of the long axis of each fragment: 10-100  
181 µm is assumed to relate to the regional fire signal and >100 µm to local fire signals (Conedera et al., 2009). ~~Charcoal~~  
182 ~~accumulation rates (particles/cm<sup>2</sup>/yr) were calculated by applying the sediment accumulation rates interpolated from the~~  
183 ~~radiocarbon age-depth model. The charcoal accumulation rate is a proxy for burned biomass which can represent changes in~~  
184 ~~the amount of biomass burned or the number of fire occurrences (Aleman et al., 2013).~~

185 Organic-walled dinoflagellate cysts (dinocysts) were identified based on Zonneveld et al. (2013), DINOFLAJ3 (Williams et  
186 al., 2017), and the online modern dinocyst determination key, viz Zonneveld and Pospelova (2015) and references therein. The  
187 percentage of each taxon was calculated based on the total number of dinocysts. ~~The 95% confidence intervals of percentages~~  
188 ~~were calculated following Maher (1972).~~ All identified dinocyst taxa and their motility affinities are listed in Table S1. In  
189 addition to the above content, foraminiferal organic linings, and other non-pollen palynomorphs such as fungal spores were  
190 counted. All counts of pollen, microcharcoal and dinocysts as well as other data discussed in this study have been submitted  
191 in the Pangaea database (<https://pangaea.de>) (Felden et al., 2023).

Formatted: Font: Italic

Formatted: Font: (Asian)+Body Asian (宋体), (Asian) Chinese (Simplified, Mainland China)

Formatted: Font: (Asian)+Body Asian (宋体), (Asian) Chinese (Simplified, Mainland China)

### 192 3.6 Statistical analysis

193 The pollen and dinocyst data were analyzed statistically using the CANOCO software (Canonical Community Ordination:  
194 version 5) (ter Braak and Smilauer, 2012). The percentage data used for statistical analysis was not transformed. A Detrended  
195 Correspondence Analysis (DCA) was first conducted to test the distribution of the dataset (unimodal or linear). The longest  
196 gradient of DCA analysis was found to be 1.1 for pollen data and 1.5 for dinocyst data with standard deviations both less than  
197 3, suggesting that the linear model is more suitable. Accordingly, separate Principal Component Analysis (PCA) were  
198 performed to determine the relationship between relative abundances of pollen and dinocyst taxa, respectively. Assemblage  
199 zones were determined using the constrained cluster analysis (CONISS) in the TILIA (3.0.1) software (Grimm, 2015), which  
200 were performed separately, including all counted for the pollen (based on a sum excluding *Pinus*) and dinocyst taxa, with the  
201 exception of The top two samples were excluded from the dinocyst CONISS analysis due to in which insufficient dinocysts  
202 counts were found.

Formatted: Font: Italic

## 203 4. Results

### 204 4.1 Age-depth model

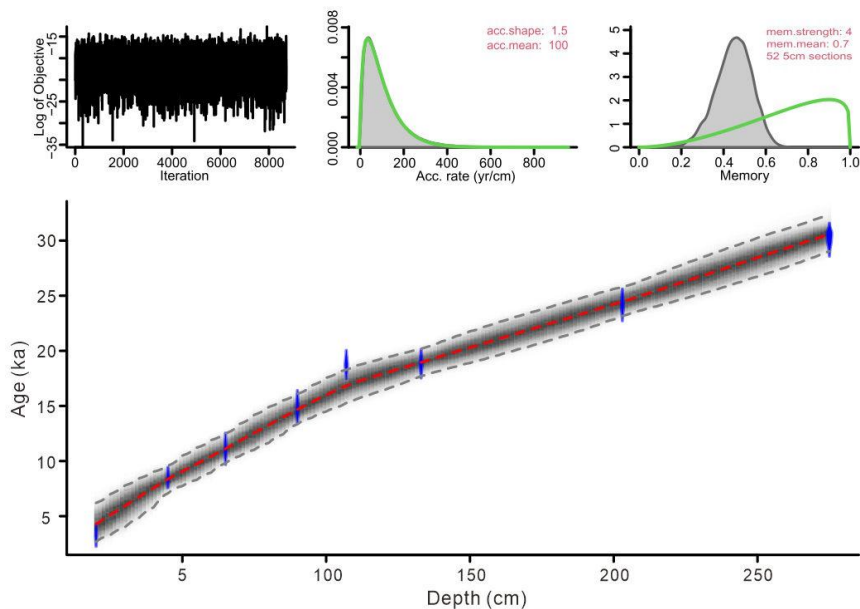
205 The eight <sup>14</sup>C AMS measurements exhibit a systematic increase in radiocarbon age with sediment depth (Table 1). The age-  
206 depth model was constructed using the eight AMS <sup>14</sup>C measurements in a Bayesian framework implemented in Bacon (Blaauw  
207 and Christen, 2011). A prior accumulation rate of 100 yr/cm (shape = 1.5, normal distribution) was applied, with the core  
208 divided into 52 depth sections of 5 cm. The default memory parameter was retained. Posterior weighted mean calibrated ages  
209 were used to derive linear sedimentation rates. The resulting model indicates a basal age of ~33 ka for core SCS GC-1, with  
210 sedimentation rates ranging between 0.005 and 0.013 cm/yr (Figs. 2 and 3a).

211

212 **Table 1:** AMS <sup>14</sup>C measurement for mixed planktonic foraminifera from the core SCS GC-1.

Lab #	Depth (cm)	Material	<sup>14</sup> C age (yr BP)	Calibrated age median (cal. yr BP)	cal. <sup>14</sup> C age (cal. yr BP, ±2σ)
GZ10650	20	mixed species	3420±25	3036	1810-4285
GZ10651	45	mixed species	8005±35	8289	7260-9443
GZ10652	65	mixed species	10055±50	10868	9533-12260
GZ10653	90	mixed species	13090±70	14708	13392-16057
GZ10654	107	mixed species	15950±70	18342	17138-19485
GZ10655	133	mixed species	16000±90	18399	17185-19555
GZ10656	203	mixed species	20540±170	23656	22496-24875
GZ10657	275	mixed species	26700±350	29977	28806-31063

213 # yr BP denote before present (1950 AD); all age data were calibrated using the software Calib.Rev.8.10 (Stuiver and Reimer,  
214 1993) and Marine 20 (Hughen et al., 2004). The standard marine reservoir age with a local modification ( $\Delta R = 71 \pm 499$  yr) in  
215 the northern South China Sea was applied (Wan and Jian, 2014).

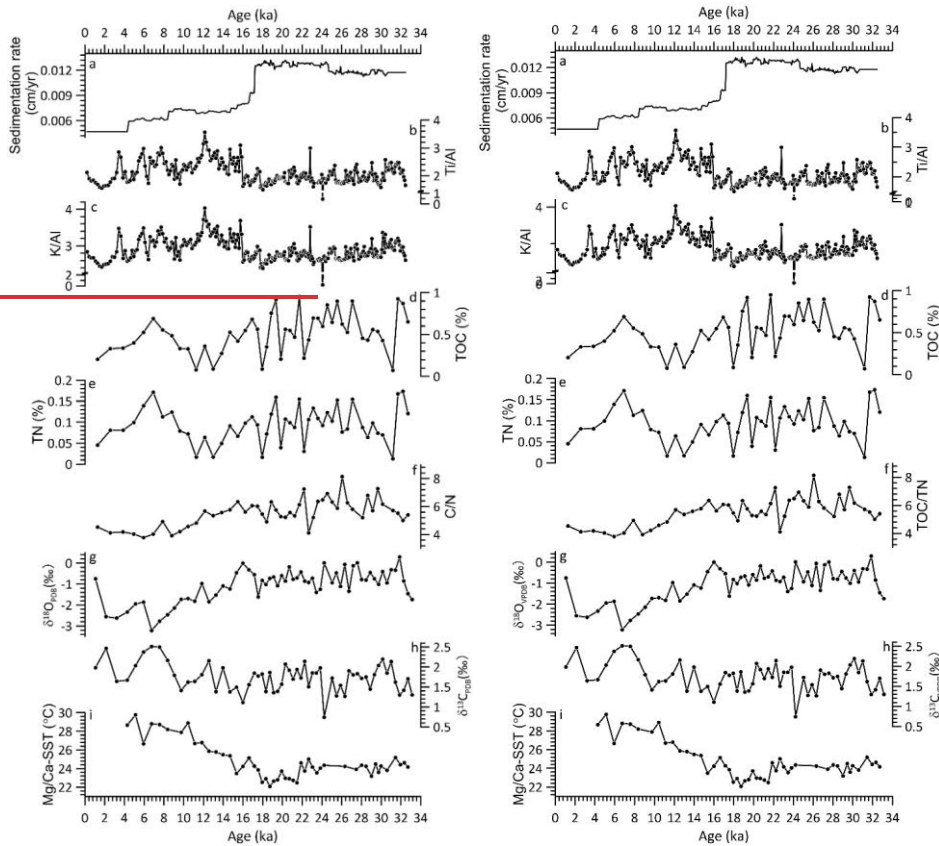


216

217 **Figure 2:** Bayesian age-depth model based on eight AMS  $^{14}\text{C}$  dates from core SCS GC-1: the blue areas represent the 95%  
 218 probability distributions of the calibrated ages; the thin red line shows the weighted mean ages, and the blackish-gray area  
 219 shows the 95% age-depth relations as modeled by the R software package Bacon 2.2 (Blaauw and Christen, 2011).

#### 220 4.2 XRF record

221 The relative contents of these six elements are found for Fe ( $5 \times 10^3$  -  $750 \times 10^3$  cps, mean =  $540 \times 10^3$  cps), Ca ( $0.7 \times 10^3$  -  $650 \times 10^3$   
 222 cps, mean =  $190 \times 10^3$  cps), K ( $1.5 \times 10^3$  -  $166 \times 10^3$  cps, mean =  $91 \times 10^3$  cps), Si ( $1 \times 10^3$  -  $144 \times 10^3$  cps, mean =  $71 \times 10^3$  cps)  
 223 followed by Ti ( $2 \times 10^3$  -  $68 \times 10^3$  cps, mean =  $41 \times 10^3$  cps) and Al ( $0.5 \times 10^3$  -  $14 \times 10^3$  cps, mean =  $6 \times 10^3$  cps) (Fig. S1). Similar  
 224 patterns among terrigenous elements Fe, K, Ti, Al and Si were observed together with a clearly opposite pattern of marine  
 225 origin element Ca. The Ti/Al and K/Al show similar patterns with significant correlation ( $r = 0.94$ ,  $P < 0.001$ ) throughout the  
 226 record (Figs. 3b and 3c), with low values prior to 16 ka and then increase quickly to much higher values after 16 ka with  
 227 gradually decreasing trend to the end of the record.



228

229 **Figure 3:** Core SCS GC-1 sedimentation rate (a), major element ratio (b-c), contents of total organic carbon (TOC, d) and  
 230 nitrogen (TN, e), TOC/TN ratio (f), stable carbon-oxygen isotope  $\delta^{18}O_{VPDB}$  (g) and oxygen-stable carbon isotope  $\delta^{13}C_{VPDB}$   
 231  $\delta^{13}C_{VPDB}$  (h) isotopes of planktic foraminifera, and Mg/Ca-SST (i).

232

#### 4.3 TOC, TN and TOC/TN record

233 TOC content and the TOC/TN ratio exhibit significant fluctuations throughout the record (Figs. 3d, 3e and 3f). The period  
 234 prior to 14.7 ka is characterized by high TOC content with low values around 31.2 ka, 22.2 ka, 19.8 ka, 17.9 ka. After 14.7 ka,  
 235 TOC decreased until 10.4 ka when it increased again to a high level around 6.9 ka followed by a decline trend until the top of  
 236 the record. Similarly, TOC/TN ratio also exhibits high values prior to 14.7 ka, which then decreased to minimum between 8.8-  
 237 5.9 ka interrupted by a brief increase around 7.9 ka.

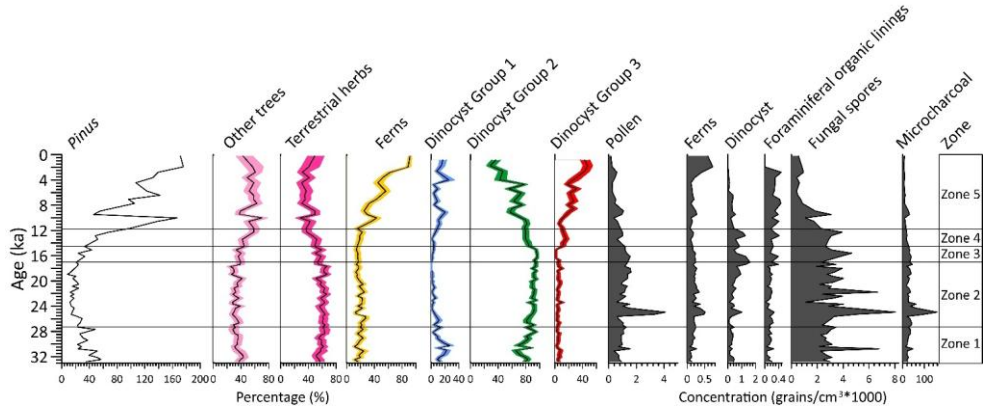
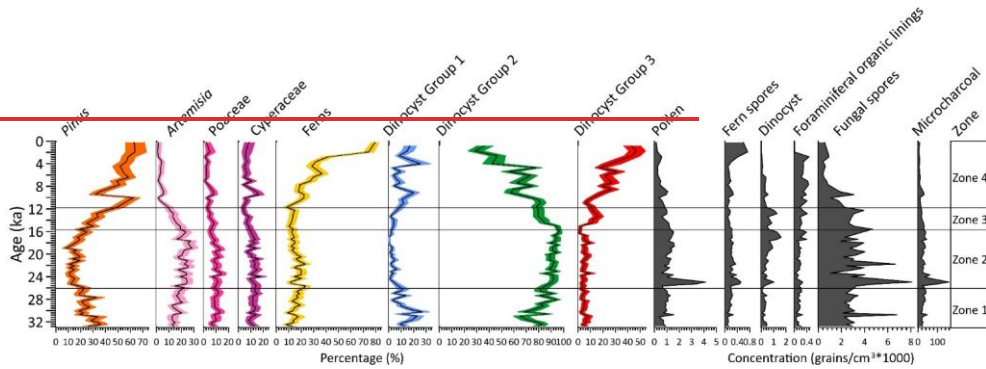
238 **4.4 Planktonic foraminiferal isotopic and Mg/Ca-SST record**

239 The  $\delta^{18}\text{O}$  values of planktonic foraminifera *G. ruber* shells range from  $-3.2\text{‰}$  to  $0.3\text{‰}$  (mean= $-1.1\text{‰}$ ) with higher values  
240 prior to 16-18.7 ka, then rapidly started decreasing to much lower values with a short decline around 17.5-14.7 ka (Fig. 3g).  
241 The  $\delta^{13}\text{C}$  values range from  $0.7\text{‰}$  to  $2.5\text{‰}$  (mean= $1.7\text{‰}$ ) with relatively low values prior to 16 ka (Fig. 3h), there after  
242 increasing but with substantial variation.

243 Mean Mg/Ca-derived SSTs range from  $22.1^{\circ}\text{C}$  to  $29.7^{\circ}\text{C}$  (mean =  $24.8^{\circ}\text{C}$ ) across the core (Fig. 3i). Relatively low values  
244 ( $23.2\text{-}25.2^{\circ}\text{C}$ , mean =  $24.2^{\circ}\text{C}$ ) occur prior to 21.9 ka, followed by a further decline to the lowest values ( $22.1\text{-}24.6^{\circ}\text{C}$ , mean =  
245  $23.1^{\circ}\text{C}$ ) between 21.9-17.5 ka. After -15-17.5 ka, SSTs increase progressively toward the highest values observed in the  
246 record ( $23.5\text{-}29.7^{\circ}\text{C}$ , mean =  $26.8^{\circ}\text{C}$ ) with a short decline around 16.6-14.7 ka.

247 **4.5 Palynological record**

248 The complete diagrams of pollen, dinocyst percentages and concentrations, and charcoal and dinocyst-results are shown in  
249 Figs. S2-and S63. Pollen preservation-concentration is variable, with particularly high concentrations ( $390\text{-}4100$  grains/ $\text{cm}^3$ ;  
250 mean =  $1200$  grains/ $\text{cm}^3$ ) prior to 16.1 ka, and highest concentrations around 25.3-25.0 ka ( $3300\text{-}4100$  grains/ $\text{cm}^3$ ; mean =  
251  $3700$  grains/ $\text{cm}^3$ ) (Fig. 4). Similarly, charcoal exhibits the highest concentrations ( $36\text{-}155\times 10^3$  particles/ $\text{cm}^3$ ; mean =  $83\times 10^3$   
252 particles/ $\text{cm}^3$ ) around 25.3-23.7 ka, decreasing after 15.6 ka, reaching minimum values at the top of the core ( $9\text{-}31\times 10^3$   
253 particles/ $\text{cm}^3$ ; mean =  $21\times 10^3$  particles/ $\text{cm}^3$ ) (Figs. 4 and S6). Dinocyst concentrations are relatively low, ranging from  $7\text{-}1600$   
254 cysts/ $\text{cm}^3$  (average of  $450$  cysts/ $\text{cm}^3$ ) with high values of  $110\text{-}1600$  cysts/ $\text{cm}^3$  (average of  $650$  cysts/ $\text{cm}^3$ ) between 25.6-11.7 ka  
255 (Figs. 4 and S5). After 11.7 ka, dinocyst concentrations decrease, reaching a minimum at the end of the record.



256

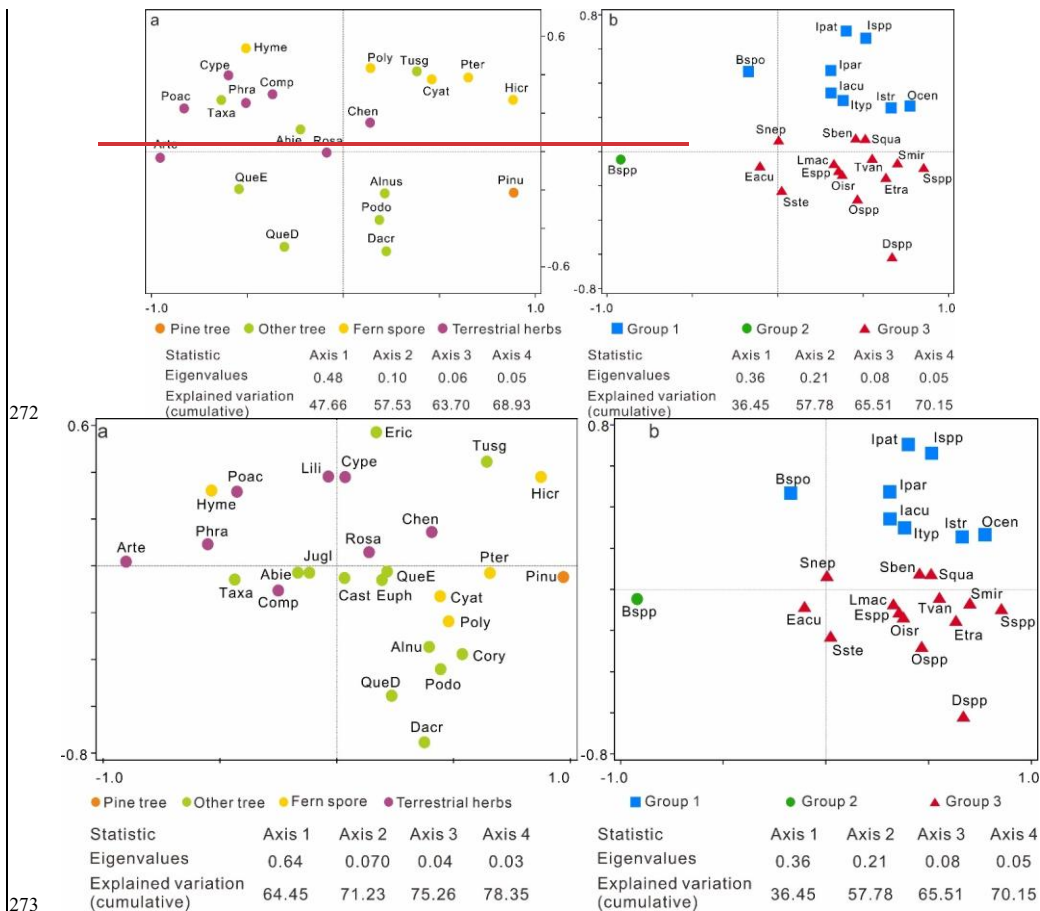
257

258 **Figure 4:** Percentages (%) of dominated pollen taxa, including ~~tree~~ pollen of *Pinus*, ~~other trees~~, terrestrial ~~herbs~~ pollen  
 259 *Artemisia*, *Poaceae* and *Cyperaceae*, fern spores, and three dinocyst groups based on principal component analysis (PCA)  
 260 analysis, concentrations (grains/cm<sup>3</sup>\*1000) of pollen, fern spores, dinocyst, foraminiferal organic linings, fungal spores and  
 261 microcharcoal concentration (particles/cm<sup>3</sup>\*1000).

262 ~~According~~ According to the PCA results (Fig. 5a), pollen and spore taxa are well-separated based on their associated biomes.  
 263 Specifically, *Pinus* and fern spore (notably *Hicriopteris*, *Pteris*, *Polypodiaceae* and *Cyathaceae*) form a distinct cluster on the  
 264 positive end of axis 1, while characteristic terrestrial herbs (particularly *Artemisia*, *Poaceae* and *Cyperaceae*) are separated  
 265 along the negative end of axis 2 ~~1 and relatively positive side of axis 2~~. Three groups of dinocyst taxa can be distinguished  
 266 based on the PCA results, showing clearly different trends across the record (Fig. 5b). Group 1: *Operculodinium centrocarpum*,  
 267 *Impagidinium* spp., *Impagidinium aculeatum*, *Impagidinium patulum*, *Impagidinium paradoxum*, *Impagidinium striatum*,  
 268 *Impagidinium* type1; *Bitectatodinium spongium*; Group 2: *Brigantedinium* spp.; Group 3: *Echinidinium* spp., *Echinidinium*  
 269 *aculeatum*, *Echinidinium transparentum*, *Selenopemphix nephroides*, *Stellasinium stellatum*; *Selenopemphix quanta*,  
 270 *Dubridinium* spp., *Operculodinium israelianum*; *Operculodinium* spp., *Lingulodinium machaerophorum*, *Tuberculodinium*  
 271 *vancampoeae*, *Spiniferites mirabilis*, *Spiniferites* spp.; *Spiniferites bentoni*.

Formatted: Font: Italic

Formatted: Font: Not Italic



274 **Figure 5:** Results of the principal component analysis (PCA) illustrating the ordination of pollen (a) and dinocyst taxa (b) from  
 275 core SCS GC-1 with colored symbols referring to the groups. For pollen, pine tree (orange): Pinu (*Pinus*); other tree (light  
 276 green): QueE (*Quercus* evergreen), QueD (*Quercus* deciduous), Alnu (*Alnus*), Podo (Podocarpaceae), Dacr (*Dacrycapus*),  
 277 Taxa (Taxaceae), Abie (*Abies*), Tusc (*Tusga*), Eric (*Ericaceae*), Jugl (*Juglans*), Cory (*Corylus*), Cast (*Castanea*), Euph  
 278 (*Euphorbiaceae*); fern spores (yellow): Hicr (*Hicriopteris*), Pter (*Pteris*), Cyat (Cyatheaaceae), Poly (Polypodiaceae), Hyme  
 279 (Hymenophyllaceae); terrestrial herbs (purple): Arte (*Artemisia*), Poac (Poaceae), Cype (Cyperaceae), Comp (Compositae),  
 280 Phra (*Phragmites*), Chen (Chenopodiaceae), Rosa (Rosaceae), Lili (*Liliaceae*); For dinocyst groups, Group 1 (blue): Ocen (*O.*  
 281 *centrocarpum*), Ispp (*Impagidinium* spp.), Iacu (*Impagidinium aculeatum*), Ipat (*Impagidinium patulum*), Ipar (*Impagidinium*  
 282 *paradoxum*), Istr (*Impagidinium striatum*), Ityp (*Impagidinium* type1); Group 2: Bspo

Formatted: Font: Italic

Formatted: Font: Italic

Formatted: Font: Italic

283 (*Brigantedinium* spp.); Group 3: Espp (*Echinidinium* spp.), Eacu (*Echinidinium aculeatum*), Etra (*Echinidinium*  
284 *transparantum*), Snep (*Selenopemphix nephroides*), Sste (*Stellasinium stellatum*); Squa (*Selenopemphix quanta*), Dspp  
285 (*Dubridinium* spp.), Oisr (*Operculodinium israelianum*); Ossp (*Operculodinium* spp.), Lmac (*Lingulodinium*  
286 *machaerophorum*), Tvan (*Tuberculodinium vancampoe*), Sben (*Spiniferites bentori*); Smir (*Spiniferites mirabilis*); Sssp  
287 (*Spiniferites* spp.).

288 Separate CONISS analysis were performed for pollen and dinocyst data, with results shown in Figs. S2 and S4. Considering  
289 that the zonations based on pollen and dinocyst data show very similar results, five main zones can be recognized in the record  
290 for the purpose of synthesizing the multi-proxy climatic signal (Fig. 4).According to the variations in percentage and  
291 concentration values of pollen, dinocyst and charcoal as well as the CONISS analysis based on the percentages of pollen and  
292 dinocyst, four zones can be recognized (Fig. S2):

#### 293 4.5.1 Zone ~~SCS-GC-1~~1 (301-2317cm, 32.8-25.67.3 ka)

294 This zone is characterized by relatively high percentages of *Pinus* and evergreen *Quercus* (evergreen), while pollen taxa of  
295 terrestrial herbs such as *Artemisia*, Poaceae and Cyperaceae as well as fern spores including *Hicriopteris*, Polypodiaceae,  
296 Cyathaceae are relatively low (Figs. 4 and Fig-S2). High fungal spore concentrations here coincide with low charcoal  
297 concentrations. The percentages of heterotrophic taxa *Brigantedinium* spp. (Group 1) increase gradually to the end of this zone,  
298 whereas the percentages of autotrophic taxa (Group 2) particularly *Impagidinium* species reach their maximum levels in the  
299 record but decline towards the end of this phase (Figs. 4 and Fig-S2S4). Concentrations of foraminiferal organic linings reach  
300 minimum in this zone.

#### 301 4.5.2 Zone ~~SCS-GC-1~~2 (2317-10997 cm, 27.35.6-15.67.0 ka)

302 The percentage of *Pinus* pollen decreases to its lowest values of the entire record. Meanwhile, terrestrial herb taxa, particularly  
303 *Artemisia*, increase to their highest levels along with fungal spores. Some fern spore types, including Polypodiaceae,  
304 Hymenophyllaceae, Cyatheaceae and *Pteris*, also exhibit relatively high values compared to Zone ~~1~~ *SCS-GC-1* (Figs. 4 and  
305 Fig-S2). Concentrations of pollen, fern spores and charcoal all reach maximum values, peaking around 25.3-24.3 ka when  
306 dinocyst concentrations also exhibit a maximum, along with *Brigantedinium* spp. On the other hand, Group 1 dinocyst taxa  
307 are at minimum values in this zone. Concentrations of foraminiferal organic linings remain at low value in this zone.

#### 308 4.5.3 Zone ~~SCS-GC-1~~3 & Zone 4 (10997-69 cm, 15.67.0-11.7 ka)

309 CONISS analysis suggests a sub-zone (zone 3) around 17.0-14.5 ka which is marked by a further decline of *Pinus* and increase  
310 in herb pollen. Then zone 4 is ~~zone~~ is characterized by the rapid increase in *Pinus* pollen, accompanied by a sharp decline in  
311 terrestrial herbs, especially *Artemisia*. Concentrations of fungal spores exhibit a declining trend and return to the levels  
312 observed in Zone ~~SCS-GC-1~~1. Concentrations of pollen, fern spores and charcoal also exhibit a declining trend to reach near  
313 the lowest levels, whereas dinocyst concentrations remain relatively prominent. However, the percentage of *Brigantedinium*  
314 spp. exhibits a decline in this zone, accompanied by a marked increase of Group 3 taxa, including *Dubridinium* spp. and  
315 *Echinidinium* spp. Meanwhile, dinocysts in Group 2 achieve relatively high values. Concentrations of foraminiferal organic  
316 linings increase gradually from the beginning of this zone.

#### 317 4.5.4 Zone ~~SCS-GC-1~~4 5 (69-0 cm, 11.7 ka-present)

318 The percentages of *Pinus* pollen reach their highest values of the entire record interrupted around 9.5-9.0 ka by a very marked  
319 decline to values close to those of Zone ~~SCS-GC-1~~1. The abrupt reduction in *Pinus* pollen is also observed in the overall  
320 pollen, fungal spore, charcoal concentration, and in terrestrial herb pollen especially. Additionally, this zone is characterized  
321 by the increase in fern spores, particularly *Hicriopteris* which exhibits a short, sharp increase around 2.8 ka (Figs. 4 and Fig-  
322 S2). The percentage of *Brigantedinium* spp. decreases to the lowest values of the entire record, whereas the percentage of  
323 Group 3 dinocyst taxa, along with the concentration of foraminiferal organic linings all reach their highest values.

Formatted: Font: Italic

## 324 5. Discussion

### 325 5.1 Environmental significance of key proxies

#### 326 5.1.1 K/Al and Ti/Al

327 In comparison to single elements, elemental ratios which are insensitive to dilution effects, are more useful as environmental  
328 indicators (Govin et al., 2012). Ti is highly enriched in mafic and volcanic rocks, while Al is a major component of most  
329 common clay mineral found in all types of weathered continental crust. The SCS is surrounded by diverse geological terrains  
330 with distinct Ti/Al ratios originating from different sources such as the Luzon Volcanic Arc (Philippines), Taiwan and other  
331 basaltic sources with high Ti/Al, while with low Ti/Al originating from the major continental river systems that drain ancient,  
332 weathered landmasses. Thus, Ti/Al can provide a robust picture of terrestrial input and its origin in the complex environment  
333 of the SCS. High Ti/Al indicates increased relative input of sediment from a volcanic or mafic source/less chemical, and low  
334 Ti/Al indicates increased relative input of sediment from a felsic continental source (e.g., Pearl River, Mekong River) (Hu et  
335 al., 2013; Wan et al., 2007). K/Al and Ti/Al records of ODP Site 1143 from the SCS generally show low values during glacial  
336 periods and high values during interglacial periods, clearly indicating that increase in K/Al and Ti/Al is probably related to  
337 wetter conditions and thus the intensified chemical weathering (Clift et al., 2008; Tian et al., 2011; Wei et al., 2004).

#### 338 5.1.2 Source area and transport of pollen and spores

339 In the northern SCS sediments, the modern distribution of tree pollen, particularly *Pinus*, shows disproportionately high  
340 representation relative to other pollen types. This suggests substantial contributions from south and southeast China,  
341 transported primarily by the northeasterly winter monsoon and associated wind-driven currents. While elevated *Pinus*  
342 percentages can signal either a strengthened winter monsoon or a cool, humid climate (Luo et al., 2018; Sun et al., 2003), PCA  
343 results (Fig. 5a) indicate that this ambiguity can be resolved by incorporating fern spore data. Unlike ~~the~~ wind-dispersed *Pinus*  
344 pollen, ~~the larger, heavier fern~~ spores ~~of ferns~~ are ~~larger, heavier, and~~ primarily transported by river runoff. Their high  
345 abundance in sediments therefore signals a proximal source from humid montane forests (e.g., in Taiwan and ~~Southern~~  
346 ~~southern~~ China), reflecting a humid climate controlled by the EASM (Kaars et al., 2000; Sun et al., 2000b; Wang et al., 2009).  
347 Consequently, a simultaneous peak in both *Pinus* pollen and fern spores is incompatible with a scenario of solely strengthened,  
348 dry winter winds. Instead, this combined signal robustly indicates a cool and humid climatic regime. ~~In this regime, where a~~  
349 ~~vigorous EASM delivered high rainfall, which (promoted ing-fern-rich vegetation and riverine spore transport,)~~ while the  
350 ~~winter monsoon~~EAWM remained active enough to distribute *Pinus* pollen without dominating the climatic regime. ~~Therefore,~~  
351 ~~we propose a possible interpretation for the low *Pinus* during the glacial period and high *Pinus* during the interglacial period:~~  
352 ~~during the glacial period especially during the LGM, a strong but dry EAWM could efficiently transported *Pinus* pollen from~~  
353 ~~distant montane source areas. However, local arid conditions on the exposed continental shelf limited the growth of conifers~~  
354 ~~near the core site leading to moderate percentages in the record; during the interglacial period especially during the Holocene,~~  
355 ~~despite the increased distance due to sea-level rise, enhanced EASM-driven humidity favoured the expansion of Pine forests~~  
356 ~~in source regions. Concurrently, altered atmospheric and oceanic circulation patterns likely facilitated the long-distance~~  
357 ~~transport of pollen to the deep basin.~~

358 *Artemisia*, Poaceae and Cyperaceae pollen are the main components of terrestrial herbs observed in the core. *Artemisia* spp. is  
359 currently widely distributed in temperate grassland and steppe which is associated with cool, semi-arid conditions (Bandara et  
360 al., 2023; Sun et al., 2003). Although Poaceae and Cyperaceae pollen indicate a range of different habitats, high percentages  
361 of Poaceae pollen in the sediment are suggestive of grassland vegetation, and a high representation of Cyperaceae pollen  
362 ~~typically can~~ points to a wetland environments, ~~though in association with *Artemisia* and Poaceae, it may also form part of dry~~  
363 ~~grassland communities~~ (Sun et al., 2003; Wang et al., 2009).

364 Previous studies have found clear temporal variations in pollen assemblages in the SCS characterized by marked higher pollen  
365 concentrations in glacial sediments than in interglacial sediments (Jiwarungruengkul and Liu, 2021; Sun et al., 2000a; Sun  
366 and Luo, 2001; Sun et al., 2003; Zheng and Lei, 1999). On one hand, the large amount of pollen in glacial sediments at the site  
367 might be transported by a strengthened northeast winter monsoon from the Asian mainland and Taiwan Island. In contrast,

Formatted: Font: Italic

Formatted: Font: Italic

Formatted: Font: Italic

Formatted: Font: Italic

368 during the last glacial low stand, sea level was 120-150 m lower than today, exposing much of the northern SCS continental  
369 shelf and increasing land area by roughly 24×104 km<sup>2</sup> (Chen et al., 2020; Sun et al., 2000a; Wang et al., 2009). The northern  
370 SCS would likely receive substantial pollen and spore amounts via wind or water from the exposed continental shelf which  
371 was covered by grassland under the prevailing dry and temperate climate of the time (Luo and Sun, 2005; Sun et al., 2003).  
372 This expansion of open, terrestrial herb-dominated vegetation likely occurred on both the exposed shelf and the adjacent  
373 continental catchments due to the overall drier glacial climate. Typically, during glacial periods, herbaceous vegetation is  
374 predominant in the region, whereas during interglacial periods tree and ferns dominate the terrestrial land mass adjacent to the  
375 SCS (Sun et al., 2000a; Sun and Luo, 2001). Such glacial-interglacial transitions are driven by changes in climate, or ocean  
376 currents, or both. During MIS 2 (21-11.5 ka), *Artemisia* increased again and occupied most of the extensive emerged  
377 continental shelf (Sun et al., 2003). Accordingly, the ratio of trees/herbs pollen is a valuable indicator of glacial-interglacial  
378 cycles along with their associated vegetation and climate conditions.

### 379 5.1.3 Dinocysts

380 Although modern dinocyst distributions are strongly correlated with sea surface conditions such as sea surface temperature,  
381 sea surface salinity, nutrient levels and productivity (Dale, 1996; Marret and Zonneveld, 2003; Zonneveld et al., 2024),  
382 dinocyst deposition and preservation in marine sediments are affected by various non-ecological, taphonomic factors which  
383 may alter the primary dinocyst accumulation in the sediment (Holzwarth et al., 2007). It is therefore crucial to account for  
384 these factors before relating the fossil dinocyst record to palaeoenvironmental conditions. Upwelling off west Luzon is driven  
385 by the EAWM and intensifies during stronger EAWM phases. This process brings nutrient-rich subsurface waters to the surface,  
386 promoting enhanced dinoflagellate production (Yuan et al., 2004b). The Kuroshio Current, which transports warm and high-  
387 salinity water into the northern SCS leading to a significant increase in sea surface temperature, is also a significant factor  
388 influencing dinoflagellate growth. Additionally, heterotrophic taxa, such as degradation-sensitive species from the  
389 *Protoperidinium* genus, are more susceptible to aerobic degradation compared to autotrophic taxa (Holzwarth et al., 2007).  
390 This may be influenced by the water oxygen content which may therefore alter dinocyst assemblages before and after  
391 sedimentation (Zonneveld et al., 2008). However, the persistent dominance of heterotrophic dinocysts in the record (up to 99%  
392 with mean values of 85%) suggests that selective dissolution of protoperidiniacean species relative to other taxa in the  
393 sediments is negligible (Zhao et al., 2017).

394 *Impagidinium* cysts as well as *O. centrocarpum* typically indicate open ocean, fully marine settings characterized by low  
395 primary productivity, low nutrient levels, and well-oxygenated bottom waters (Zonneveld et al., 2013; Zonneveld and  
396 Pospelova, 2015). Modern surface dinocyst distribution in SCS shows that most of *Impagidinium* species, *Nematosphaeropsis*  
397 *labyrinthus* and *Polysphaeridium zoharyi* are positively correlated with water depth. Their highest abundances were observed  
398 in the northern slope-deep basin which is influenced by the Kuroshio Current, indicating an open-ocean environment (Li et al.,  
399 2020). In the northern Philippine Sea, the predominance of *Impagidinium* taxa from the bottom sediments is also indicative of  
400 pelagic and tropical regions (Matsuoka, 1981). During winter, the Kuroshio Current transports high-salinity, low-nutrient  
401 waters from the Philippine Sea through the Luzon Strait, which then flows along the continental shelf break, reaching the study  
402 area in the northern SCS. This provides further evidence that the increased abundance of Group 1 taxa may reflect typical  
403 nutrient-poor open ocean environments and enhanced influence of the Kuroshio Current. Dinocysts preserved in SCS GC-1  
404 are dominated by *Brigantedinium* spp. (28-96%, mean = 80%), which have also been observed from sediment trap samples in  
405 the southwest Taiwan waters of the SCS with high representation ranging from 68% to 91% (Li et al., 2018b). High abundances  
406 of *Brigantedinium* spp. are characteristic of increased nutrient supply (Dale, 1996), which has been used as an indicator of  
407 primary productivity (Li et al., 2020; Zonneveld et al., 2013). In addition, *Brigantedinium* spp. is usually more abundant near  
408 the winter upwelling zone in the South China Sea (Li et al., 2020). Therefore, Group 2 taxa, characterized by the dominance  
409 of *Brigantedinium* spp., indicates intensified upwelling conditions with strong terrigenous influence that contrasts with open-  
410 ocean oligotrophic conditions indicated by Group 1. The stratigraphic variation of Group 2 cysts (Fig. 6h) displays an inverse  
411 relationship with Mg/Ca-SST, supporting the glacial 'high-productivity/low-temperature' paradigm. Group 3 taxa,  
412 characterized by dinocysts such as *Echinidinium* spp. and *S. quanta* are typically adapted to fully marine, eutrophic, and highly  
413 productive regimes, and are likely indicative of water column stratification and upwelling processes in open ocean  
414 environments (Zonneveld et al., 2013). The shift from Group 2 to Group 3 dominance during the deglaciation may thus signal  
415 a transition from terrestrial nutrient-driven productivity to a more stratified, marine-dominated productivity regime.

Formatted: Font: (Asian)+Body Asian (宋体), (Asian) Chinese  
(Simplified, Mainland China)

## 5.2 Sea-level forcing Shelf exposure, aridity and high marine productivity during the LGM

Over the past 33 ka, four different periods distinct climatic phases have been clearly recognized based on our multi-proxy record (Fig. 6): pre-LGM (32.8-25.27, 6.3 ka), LGM (25-67.3-15-67.0 ka), last deglaciation (17.0-11.7 ka) which includes the Heinrich Stadial 1 (H1, 17.0-14.5 ka), (15.6-11.7 ka) and the Holocene (11.7 ka-present). This sequence indicating reveals a distinctive pattern of pronounced glacial-interglacial transition. The pre-LGM phase already exhibited features of a cooler and drier glacial regime, which became more pronounced during the LGM. This period was characterized by markedly higher sedimentation rates (Fig. 3a), cooler SST (Figs. 6c and 6d), higher primary productivity (Figs. 6e and 6h), reduced humidity (Figs. 6f, 6j, 6l and 6m), a landscape predominance of terrestrial herbs dominated by herbaceous vegetation (Fig. 6j), and strengthened fire activity (Fig. 6k) which became more pronounced during the LGM.

During the LGM, sea levels were approximately 120 m lower than present, leading to extensive exposure of the northern SCS continental shelf (Fig. 6b), which effectively extended the coastal plains and created an expansive, low-relief terrestrial surface (Hanebuth et al., 2000). While previous studies have suggested that attributed elevated charcoal and terrestrial pollen concentrations during the LGM reflect to the reduced distance to the sediment sources associated with the exposure of the northern SCS from this exposed continental shelf during glacial low stands (Luo and Sun, 2005; Sun et al., 2000a), our multi-proxy data supports support this interpretation proximal-source effect and further demonstrate that the vegetation colonizing the shelf was fundamentally shaped by the cold and dry glacial climate. Specifically, the minimum tree/herb ratio (Fig. 6j) indicates extensive expansion of herbaceous vegetation the high percentages of terrestrial herb pollen, in particular arid-tolerant *Artemisia* together with Poaceae and Cyperaceae, minimum tree pollen (Fig. S2), and trees/herbs ratio (Fig. 6j) all indicate a herbaceous landscape. Moreover, independent climate proxies also confirm the arid conditions: the low K/Al ratio (Fig. 6f) suggesting reduced chemical weathering under drier conditions, aligns with the enriched speleothem  $\delta^{18}\text{O}$  values indicating a weakened EASM and reduced rainfall over the region (Fig. 6l) (Cheng et al., 2016). This aridity suppressed forest growth and favoured drought-tolerant herbs. Concurrently, the maximal concentrations of microcharcoal (Fig. 6k), especially the large charcoal particles ( $>100\ \mu\text{m}$ ) indicative of local fires (Fig. S6), coincide with maximal herb pollen. This is ecologically explainable: herbaceous vegetation especially in dry seasonal climate could produce fine, highly flammable fuel that supports frequent and potentially high-intensity fires. Therefore, the high terrestrial herb pollen percentage reflects a dual control: the exposed shelf provided a vast proximal source area, while the glacial climate determined that this area and possibly the adjacent continental catchments would be occupied by drought-adapted grassland/steppe vegetation.

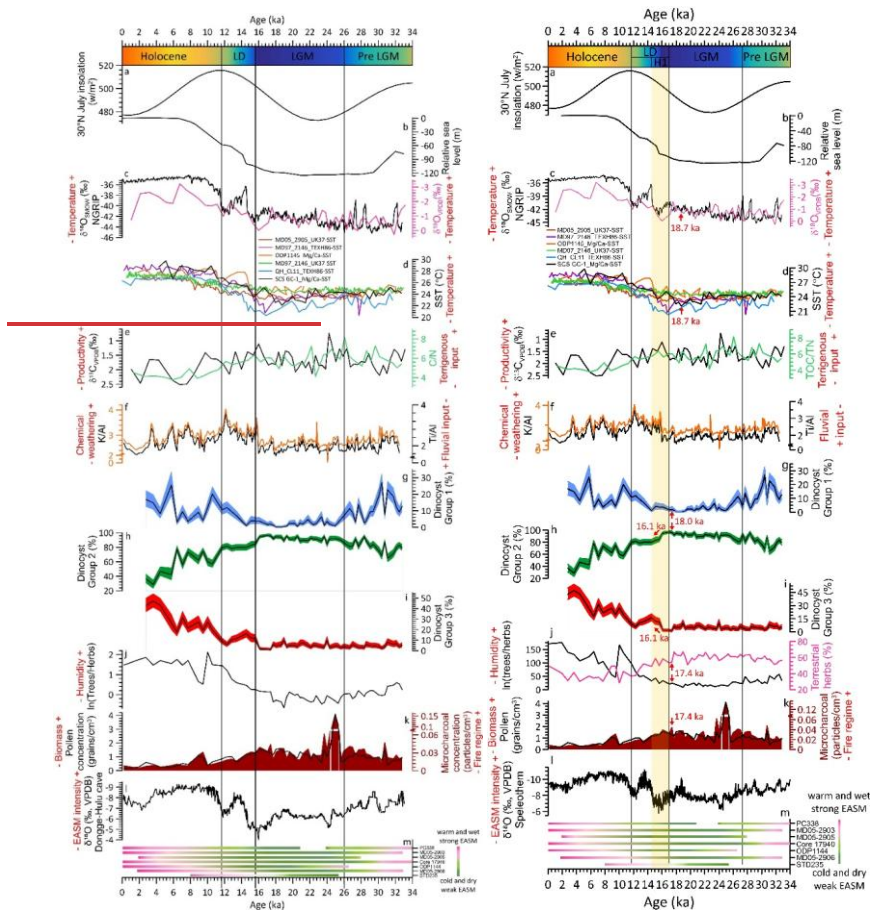
The substantially shortened distance between the exposed shelf and the core site (Lambeck et al., 2014) would have facilitated more efficient transfer of terrigenous nutrients to proximal deep-sea areas. The low Ti/Al ratios (Fig. 6f) suggest that this enhanced input originated mainly from felsic continental rivers (e.g., the Pearl River). Although weakened EASM would typically suppress fluvial discharge, this effect appears to have been offset by the closer coastline and the likely persistence of eolian dust transport from the arid Chinese mainland, at the expense of *Pinus* on the exposed shelf surface, which would have supplied abundant fuel, consistent with the high pollen concentrations (Fig. 6k) and the increased abundance of large charcoal particles ( $>100\ \mu\text{m}$ ) (Fig. S3) representing predominantly local fires. Concurrently, this open landscape, combined with likely enhanced erosion under such variable glacial conditions would have supplied abundant terrestrial nutrients to the adjacent ocean. Enhanced terrigenous nutrient delivery from this expansive, herb-covered continental shelf and arid continental hinterlands also appears to have stimulated elevated marine productivity during the LGM. This is clearly recorded in our marine proxies: TOC/TN ratio with a range between 3.8-8.1 throughout the record indicates a marine phytoplankton-dominated organic matter source (Meyers, 1999), while elevated  $\delta^{13}\text{C}$  values of planktonic foraminifera (Fig. 6e) during this period suggest enhanced organic carbon export. Critically, the combined fluvial and eolian nutrient fluxes would have created a nutrient-replete surface ocean, directly favouring heterotrophic dinoflagellates such as *Brigantedinium* (Smayda and Trainer, 2010). This can thereby well explain the dinocyst record characterized by pronounced dominance of increased dinocyst Group 2 (*Brigantedinium* spp. which can constitute up to 97%, mean = 81%) indicative of high nutrient availability, alongside the near-absence of and reduced oligotrophic, open-ocean Group 1 Group 1 (Figs. 6g and 6-h), together with rising TOC/TN (Fig. 6e), all points to a productivity regime sustained by abundant strengthened-terrestrial nutrient supply rather than open-ocean processes. A-This pattern is consistent with global compilations further showings that OC-organic carbon accumulation rates during glacial maxima were ~50% higher than interglacial intervals (Cartapanis et al., 2016), indicate a weakened EASM that would typically suppress fluvial discharge, this ap

Formatted: Not Highlight

Formatted: Font: Italic

464 productivity to intensified winter monsoon winds, enhanced water-column mixing, upwelling, and increased land-derived  
465 nutrient supply (Li et al., 2008). Our dinocyst record, characterized by the dominance of a heterotrophic, highly nutrient-  
466 dependent taxon, strongly supports the interpretation that terrestrial nutrient supply was a key mechanism together with the  
467 complementation of the physical forcing of strengthened winter monsoon-driven mixing.

468 ~~The substantially shortened distance between the exposed shelf and the core site (Lambeek et al., 2014) would have facilitated~~  
469 ~~more efficient transfer of terrigenous nutrients to proximal deep-sea areas. The low Ti/Al ratios (Fig. 6f) suggest that this~~  
470 ~~enhanced input originated mainly from felsic continental rivers (e.g., the Pearl River). Although the reduced K/Al (Fig. 6f)~~  
471 ~~and Donge-Hulu cave  $\delta^{18}\text{O}$  records (Fig. 6l) (Wang et al., 2001; Yuan et al., 2004a) indicate a weakened EASM that would~~  
472 ~~typically suppress fluvial discharge, this appears to have been offset by the markedly closer coastline and the likely persistence~~  
473 ~~of eolian dust transport from the Chinese mainland. The combined effect of these terrestrial nutrient sources would have~~  
474 ~~favoured heterotrophic dinoflagellate production (Smayda and Trainer, 2010), contributing to the observed rise in marine~~  
475 ~~productivity. Independent evidence from the northern SCS similarly links higher glacial productivity to intensified winter~~  
476 ~~winds, enhanced water-column mixing, and upwelling, as well as increased land-derived nutrient supply (Li et al., 2008).~~



477

478 **Figure 6:** 30°N July insolation (Laskar et al., 2004) (a); relative sea level on the Sunda Shelf, South China Sea (Hanebuth et  
 479 al., 2000) (b); NGRIP  $\delta^{18}\text{O}_{\text{SMOW}}$  (Andersen et al., 2004) (c, black) and stable oxygen  $\delta^{18}\text{O}_{\text{VPDB}}$  of planktonic foraminifera from  
 480 SCS GC-1 (c, pink); SST records from MD052905 (Zhou et al., 2012), MD972146 (Lin et al., 2014), ODP1145 (Oppo and  
 481 Sun, 2005), QHCL11 (Liu et al., 2020) and SCS GC-1 (d); stable carbon  $\delta^{13}\text{C}_{\text{VPDB}}$  of planktonic foraminifera (e, black) and  
 482 TOC/TN ratio (e, green); major element ratio Ti/Al (f, black) and K/Al (f, orange), percentages of three dinocyst groups (g, h,  
 483 i); ratio of trees/herbs (j, black) and percentages of terrestrial herbs (j, pink); pollen concentration (k, black) and microcharcoal  
 484 concentration (k, dark red shading); compilation of speleothem  $\delta^{18}\text{O}_{\text{VPDB}}$  values from central China (l) (Cheng et al., 2016);  
 485 summary of records indicating climate and potential intensity of EASM (m) (Sun et al., 2000a; Sun et al., 2000b; Luo and Sun,  
 486 2005; Zhou et al., 2012; Xie et al., 2014; Dai and Weng, 2015; Dai et al., 2015a; Yu et al., 2017; Li et al., 2019). Pre LGM:

487 pre Last Glacial Maximum; LGM: Last Glacial Maximum; LD: last deglaciation; H1: Heinrich Stadial 1. Red arrows indicate  
488 the onset of the transition in different proxies.

Formatted: Font: (Asian)+Body Asian (宋体), (Asian) Chinese (Simplified, Mainland China)

### 489 5.3 Early ocean warming, Dominance of ocean forcing, monsoon intensification and ecosystem response since the last 490 deglaciation

491 Since the last deglaciation, the northern SCS has experienced a comprehensive environmental transformation characterized by  
492 decreasing sedimentation rates, rising SST, declining primary productivity, increased moisture availability, a pronounced  
493 expansion of pine forests, and minimal-reduced fire activity. Critically, our record reveals that the initial signal of this  
494 transformation was an SST increase at ca. 18.7 ka (Figs. 6c and 6d) (Andersen et al., 2004; Lin et al., 2014; Liu et al., 2020;  
495 Oppo and Sun, 2005; Zhou et al., 2012). A key observation is that SST warming in the northern SCS which began ~1.9-3  
496 ka earlier than changes the major shifts in terrestrial vegetation and recorded by the other sediment proxies (ca. 17.4 ka, Figs.  
497 6j and 6k) (Figs. 6c and 6d) (Andersen et al., 2004; Lin et al., 2014; Liu et al., 2020; Oppo and Sun, 2005; Zhou et al., 2012).  
498 This early ocean warming provides direct, local evidence for the primacy of ocean-atmosphere forcing in initiating the regional  
499 deglacial transition. Additionally, the millennial-scale event of H1 (17.0-14.5 ka) is embedded within the early phase of this  
500 warming, recorded as an interval of low SST, high  $\delta^{18}\text{O}_{\text{VPDB}}$  of planktonic foraminifera and high percentages of terrestrial herb  
501 pollen. This suggests that short-period cold and dry conditions linked to North Atlantic forcing temporarily modulated but did  
502 not override the underlying tropical warming trend in the study area (Clark et al., 2012).

Field Code Changed

Field Code Changed

Formatted: Subscript

503 This earlier onset of SST warming corresponds more closely with rising boreal summer insolation (Fig. 6a) (Laskar et al.,  
504 2004) than with the rate of sea-level rise (Fig. 6b) (Hanebuth et al., 2000). This implies that, in addition to the well-recognized  
505 role of sea-level rise, tropical ocean warming, likely amplified by ocean-atmosphere feedbacks, acted as an initial trigger  
506 for subsequent environmental changes. This effect is especially pronounced in the tropics and is consistent with the concept  
507 of tropical ocean-atmosphere forcing (Cheng et al., 2019; Xie et al., 2010).

Field Code Changed

508 For instance, seminal work has shown that the timing of peak East Asian Monsoon intensity differs between marine and  
509 terrestrial records (An et al., 2000). Furthermore, while terrestrial pollen records from East Asian indicate rapid warming  
510 around 15 ka, synchronous with Greenland ice core and stalagmite records from southern China, marine SST reconstructions  
511 (based on Mg/Ca-SST and long chain alkenone  $\text{U}_{37}^{\text{K}}$ -SST) from the same record indicate that SSTs began to rise as early as  
512 20-19 ka, a trend more consistent with the early warming of the Western Pacific Warm Pool (Xu et al., 2013). This 3-4 kyr lag  
513 of terrestrial warming behind western Pacific oceanic warming highlights the differential thermal response and reinforces the  
514 interpretation that early ocean warming served as a critical forcing mechanism.

Formatted: Superscript

Formatted: Subscript

515 This earlier onset corresponds more closely with rising insolation (Fig. 6a) (Laskar et al., 2004) than with sea-level rise (Fig.  
516 6b) (Hanebuth et al., 2000). This implies that, in addition to the well-recognized role of sea-level rise, ocean warming likely  
517 acted as an initial trigger for subsequent environmental changes. This effect is especially pronounced in the tropics and is  
518 consistent with the concept of tropical ocean-atmosphere forcing (Cheng et al., 2019; Xie et al., 2010).

Field Code Changed

519 The sequence of multi-proxy changes in our record reveals a clear mechanistic chain initiated by this early SST rise. The  
520 mechanisms underlying these changes can be traced through both marine and terrestrial proxies. The first detectable response  
521 in our marine proxies is a shift in dinocyst assemblages at ca. 18.0 ka, marked by the incipient increase of oligotrophic Group  
522 1 dinocysts and the onset of decline in the highly nutrient-dependent Group 2 dinocysts. We attribute this to a direct  
523 oceanographic response to warming: enhanced upper water column stratification reduced vertical nutrient supply, favoring  
524 oligotrophic taxa over heterotrophic ones. Subsequent to this initial marine response, the physical reconfiguration of the  
525 coastline due to sea level rise further modulated the environmental trajectory. The inundation of the exposed continental shelf  
526 increased the distance from terrestrial sediment sources to the core site (Luo and Sun, 2005; Sun et al., 2000a) and created a  
527 sediment trap on the newly formed shallow marine environments, leading to a dramatic reduction in terrigenous material  
528 reaching our deep basin site (Liu et al., 2003; Wang and Sun, 1994). This is reflected in markedly lower sedimentation rates  
529 and increased Ti/Al ratios (Figs. 3a and 6f), indicating reduced terrestrial input. The combination of sustained ocean warming  
530 and reduced nutrient supply further suppressed heterotrophic dinoflagellates such as *Brigantidium* (Smayda and Trainer,  
531 2010), driving a pronounced decline in Group 2 dinocysts from 16.1 ka and a concurrent increase in Group 3 dinocysts which  
532 is indicative of more stratified, marine-dominated conditions (Figs. 6h and 6i), coincident with a reduction in TOC/TN (Fig.

533 6e). This shift marks a fundamental transition in the productivity regime: from a terrigenous nutrient-driven regime (Group 2  
534 dominated during the LGM) to a more stratified, marine-dominated regime (Group 3).

535 The rising sea level reduced the extent of the exposed continental shelf, increasing the distance from terrestrial sediment  
536 sources to the core site (Luo and Sun, 2005; Sun et al., 2000a). Inundation of the continental shelf created a massive sediment  
537 trap in newly formed shallow marine environments, leading to a dramatic reduction in terrigenous material reaching the deep  
538 basin (Liu et al., 2003; Wang and Sun, 1994). This is reflected in markedly lower sedimentation rates and increased Ti/Al  
539 ratios (Figs. 3a and 6f), indicating reduced terrestrial input. At the same time Parallel to these oceanic changes, the shrinkage  
540 shrinking of the continental shelf area also constrained the growth habitat for of terrestrial herbs herbaceous vegetation.  
541 Concurrently, the intensification of the EASM, a large-scale atmospheric response like initiated and reinforced by the warming  
542 tropical ocean and the evolving land-sea thermal contrast, is recorded by the rapid negative shift in the speleothem  $\delta^{18}\text{O}$  records  
543 (Fig. 6l) (Cheng et al., 2016), and is further supported by other multiple paleorecords from the northern SCS (Fig. 6m) (Dai  
544 and Weng, 2015; Dai et al., 2015; Li et al., 2019; Luo et al., 2015; Sun et al., 2000a; Sun et al., 2000b; Xie et al., 2014; Yu et al.,  
545 al., 2017; Zhou et al., 2012). This strengthened monsoon brought increased moisture to the region, supporting the ,which were  
546 progressively replaced by expanding expansion of pine forests and ferns (Figs. 5-4 and 6j) and leading to a sharp reduction in  
547 fire activity, as evidenced by decreased charcoal concentrations (Fig. 6k).

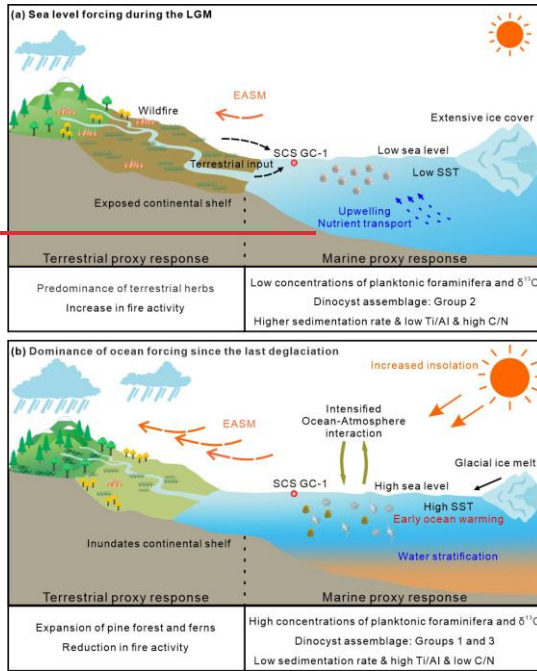
548 Additional evidence supports this ecosystem-scale reorganization. Relatively high concentrations of foraminiferal organic  
549 linings (Fig. 4) also imply indicate that the water depth and the open ocean environments had become suitable for planktonic  
550 foraminifera (Tyszka et al., 2021), while .The synchronous strengthening of the EASM, likely initiated by intensified ocean-  
551 atmosphere interactions, is reflected by the rapid negative shift in the Dongge-Hulu Cave  $\delta^{18}\text{O}$  record (Fig. 6l) (Wang et al.,  
552 2001; Yuan et al., 2004a), and is further supported by other paleorecords from the northern SCS (Fig. 6m) (Dai and Weng,  
553 2015; Dai et al., 2015; Li et al., 2019; Luo et al., 2015; Sun et al., 2000a; Sun et al., 2000b; Xie et al., 2014; Yu et al., 2017;  
554 Zhou et al., 2012). This further supported the vegetation shift by enhancing regional humidity. The wetter conditions led to a  
555 sharp reduction in fire activity, as evidenced by decreased charcoal concentrations (Fig. 6k), while the decline in coprophilous  
556 fungal spores suggests an ecosystem-level response in herbivore populations to the changing landscape (Fig. 4) (Lee et al.,  
557 2022) suggests a corresponding response in herbivore populations to the changing landscape (Fig. 4). Similar conditions  
558 patterns with increased in fern spores, decreased in terrestrial herbs and reduced dinocyst concentrations were also recorded  
559 from 12.5-6.8 ka in the core GLW31D from the northern SCS (Li et al., 2017).

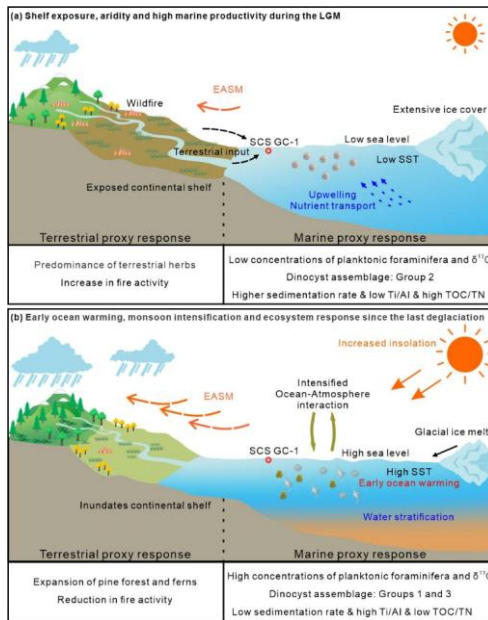
560 Likewise, reduced terrestrial input cannot fully explain the marine environmental changes particularly the decreased primary  
561 productivity and shift in dinocyst associations. The early onset of SST warming may have strengthened upper water column  
562 stratification, thereby reduced vertical nutrient supply and contributed to the decline in primary productivity. This  
563 interpretation is supported by the shift in dinocyst assemblages: Group 2 taxa decreases while Group 3 increases, consistent  
564 with more strongly stratified conditions and reduced upwelling relative to the LGM. PAdditionally, periodic peaks in  
565 oligotrophic, open-ocean dinocyst Group 1, particularly around 10.6 ka and 5.8 ka (Fig. 6g), further point to short  
566 enhancements of the an enhanced influence of the warm, nutrient-poor Kuroshio Current intrusion (Liu et al., 2016b), which  
567 would additionally further suppressed productivity in the northern SCS. Independent evidence for strengthened Kuroshio  
568 intrusion during the early Holocene is also recorded in core GLW31D from the northern SCS (Li et al., 2021).

569 Collectively, the our multi-proxy dataset shows demonstrates that the deglacial environmental transitions in the northern SCS  
570 reflects the combined action and interaction of several forcings rather than a single dominant driver complex interplay of  
571 multiple forcings (Fig. 7). The sequence began with tropical ocean warming, evidenced by the early rise in SST, which initiated  
572 the deglacial transition. Tropical ocean his warming initiated the deglacial transition through both direct directly altered marine  
573 conditions (stratification, productivity) and throughout influence and remote ocean-atmospheric feedback interactions, helped  
574 triggering the intensification of the EASM. These primary changes were then amplified and modulated by the physical effects  
575 of sea-level rise (altered sediment transport and coastal geography), a marked shift in dinocyst associations and decreased  
576 primary productivity through enhanced water column stratification. This was followed by sea level rise that reconfigured  
577 coastal geography and sediment transport, further reducing terrestrial nutrient input. The superimposed intensification of the  
578 EASM then completed the regional shift to humid conditions, driving vegetation succession and suppressing fire activity. This  
579 multi-mechanism framework highlights the northern SCS as a sensitive region where the coherent yet time-transgressive

Field Code Changed

|580 ~~complex yet coherent~~ responses of ~~both~~ marine and terrestrial systems to global climatic changes are clearly recorded during  
581 the last deglaciation.





583

584 **Figure 7:** A conceptual framework of driving mechanisms and associated environmental responses during the LGM (a) and  
 585 since the last deglaciation (b) based on multi-proxy record from the core SCS GC-1 in the northern SCS.

## 586 6 Conclusions

587 Our multi-proxy reconstruction from the northern SCS provides a high-resolution record of clear glacial-interglacial climatic  
 588 and oceanic transitions over the past 33 ka. Four distinct climatic phases are identified, viz. the pre-Last Glacial Maximum  
 589 (32.8-25-67.3 ka), Last Glacial Maximum (25-67.3-15-67.0 ka), last deglaciation (including the Heinrich Stadial 1) (15-67.0-  
 590 14-71.7 ka) and the Holocene (11.7 ka-present). The glacial intervals (pre-LGM and LGM) were characterized by higher  
 591 sedimentation rates, cooler SST, higher primary productivity, herb-dominated landscapes, reduced humidity and intensified  
 592 fire activity. This regime was primarily shaped by the effects of glacial low sea-level stand and arid climatic conditions, which  
 593 together promoted the expansion of open vegetation and enhanced the supply of terrestrial nutrients, thereby stimulating marine  
 594 productivity. A fundamental regime shift occurred during the last deglaciation, marked by evidently decreasing sedimentation  
 595 rates, rising SST, declining primary productivity, a pronounced expansion of pine forests, increased moisture availability, and  
 596 diminished fire activity. The early onset of SST warming (1.3 ka ahead of terrestrial shifts), points to tropical ocean-  
 597 atmospheric interactions as the initial trigger for the deglacial transition. The Holocene was characterized by a period of relative  
 598 stability, defined by the lowest sedimentation rates, warmest SST, highest humidity, maximum pine forest coverage and  
 599 minimal fire disturbance. In summary, the combined evidence reveals that the deglacial-environmental changes of the northern  
 600 SCS since the last glacial period reflects a shift in the dominant climate forcing mechanisms. During the glacial period, the  
 601 system was governed by the combined forcing of low sea level and continental aridity, which amplified land-sea interactions  
 602 and maintained high marine productivity. Since the last deglaciation, the climate dynamics have transitioned to a regime where

603 low-latitude processes, initiated by early ocean warming and subsequent ocean-atmosphere coupling, became the primary  
604 driver, leading to monsoon intensification and thereafter ecosystem reorganization, were driven by the interplay of multiple  
605 forcings including increased insolation, sea-level rise and monsoon intensification, with ocean warming preceding other  
606 changes, suggesting the important role of tropical ocean-atmosphere interactions in initiating this transition. This study  
607 highlights the value of integrated land-sea proxies in deciphering complex climate interactions and underscores the northern  
608 SCS's sensitivity to both high- and low-latitude forcing. Future research employing a spatial network of cores across the SCS  
609 will be crucial to better resolve the spatial patterns and teleconnections of these changes.

#### 610 **Author Contributions**

611 Xueqin Zhao: Conceptualization, Data curation, Formal analysis, Funding acquisition, Investigation, Methodology, Project  
612 administration, Supervision, Validation, Writing – original draft, Writing – review and editing; Shengjie Ye: Investigation,  
613 Visualization, Writing – review and editing; Jiahui Yao: Investigation, Formal analysis, Writing – review and editing; Michael  
614 Meadows: Validation, Writing – review and editing; Chengyu Weng: Validation, Writing – review and editing; Yasong Wang:  
615 Visualization, Writing – review and editing; Mingxing Zhang: Investigation; Yunping Xu: Conceptualization, Writing – review  
616 and editing.

#### 617 **Competing Interests**

618 The authors declare that they have no conflict of interest.

#### 619 **Acknowledgments**

620 This work was supported by the National Natural Science Foundation of China (42206048). We would like to thank the captain,  
621 crew and especially all scientists of the R/V Songhang (Shanghai Ocean University) cruise for recovering the samples. Thank  
622 Xiaodi Lu and Yinwei Xi for the sampling and helping to measure XRF. Thank Xiaodi Lu for the assistance with lab analysis.  
623 Mike E. Meadows acknowledges financial support from the Jiangsu Provincial Government Overseas Talent 100 Plan,  
624 SBX2021010183.

#### 625 **Data Availability**

626 Data used in this study has been submitted-stored in the Pangaea database (<https://www.pangaea.de>) with specific DOI:  
627 <https://doi.pangaea.de/10.1594/PANGAEA.987882> for pollen and spore, <https://doi.pangaea.de/10.1594/PANGAEA.987861>  
628 for organic-walled dinoflagellate cyst, ~~and~~ <https://doi.pangaea.de/10.1594/PANGAEA.987870> for microcharcoal,  
629 <https://doi.pangaea.de/10.1594/PANGAEA.989845> for organic carbon and nitrogen content,  
630 <https://doi.pangaea.de/10.1594/PANGAEA.989928> for foraminifera stable carbon and oxygen isotopes, and  
631 <https://doi.pangaea.de/10.1594/PANGAEA.989846> for X-ray fluorescence (XRF) scanning data.

Formatted: Default Paragraph Font

Formatted

#### 632 **References**

633 Aleman, J. C., Blarquez, O., Bentaleb, I., Bonté, P., Brossier, B., Carcaillet, C., Gond, V., Gourlet - Fleury, S., Kpolita, A.,  
634 Lefèvre, I., Oslisly, R., Power, M. J., Yongo, O. D., Bremond, L., and Favier, C.: Tracking land-cover changes with  
635 sedimentary charcoal in the Afrotropics. *Holocene*, 23, 1853-1862, doi: 10.1177/0959683613508159, 2013.  
636 An, Z.: The history and variability of the East Asian paleomonsoon climate. *Quat. Sci. Rev.*, 19(1), 171-187, doi: S0277-  
637 3791(99)00060-8, 2000.

- 638 [An, Z., Porter, S. C., Kutzbach, J. E., Xihao, W., Suming, W., Xiaodong, L., Xiaoqiang, L., and Weijian, Z.: Asynchronous](#)  
639 [Holocene optimum of the East Asian monsoon. \*Quat. Sci. Rev.\*, 19\(8\), 743-762, doi: 10.1016/S0277-3791\(99\)00031-1,](#)  
640 [2000.](#)
- 641 Andersen, K. K., Azuma, N., Barnola, J. M., Bigler, M., Biscaye, P., Cailion, N., Chappellaz, J., Clausen, H. B., Dahl-Jensen,  
642 D., Fischer, H., Flückiger, J., Fritzsche, D., Fujii, Y., Goto-Azuma, K., Grønbold, K., Gundestrup, N. S., Hansson, M.,  
643 Huber, C., Hvidberg, C. S., Johnsen, S. J., Jonsell, U., Jouzel, J., Kipfstuhl, S., Landais, A., Leuenberger, M., Lorrain, R.,  
644 Masson-Delmotte, V., Miller, H., Motoyama, H., Narita, H., Popp, T., Rasmussen, S. O., Raynaud, D., Rothlisberger, R.,  
645 Ruth, U., Samyn, D., Schwander, J., Shoji, H., Siggard-Andersen, M. L., Steffensen, J. P., Stocker, T., Sveinbjörnsdóttir,  
646 A. E., Svensson, A., Takata, M., Tison, J. L., Thorsteinsson, T., Watanabe, O., Wilhelms, F., White, J. W. C., and North  
647 Greenland Ice Core Project, m.: High-resolution record of Northern Hemisphere climate extending into the last  
648 interglacial period. *Nature*, 431(7005), 147-151, doi: 10.1038/nature02805, 2004.
- 649 Bandara, G., Luo, C. X., Chen, C. X., Xiang, R., Herath, D. B., Yang, Z. J., and Thilakanayaka, V.: Sedimental pollen records  
650 in the northern South China Sea and their paleoenvironmental significance. *J. Asian Earth Sci.*, 241, Article 105457, doi:  
651 10.1016/j.jseas.2022.105457, 2023.
- 652 Barker, S., Greaves, M., and Elderfield, H.: A study of cleaning procedures used for foraminiferal Mg/Ca paleothermometry.  
653 *Geochem. Geophys. Geosyst.*, 4(9), doi: 10.1029/2003GC000559, 2003.
- 654 Blaauw, M., and Christen, J. A.: Flexible paleoclimate age-depth models using an autoregressive gamma process. *Bayesian*  
655 *Anal.*, 6(3), 457-474, 418, doi: 10.1214/11-BA618, 2011.
- 656 Cartapanis, O., Bianchi, D., Jaccard, S. L., and Galbraith, E. D.: Global pulses of organic carbon burial in deep-sea sediments  
657 during glacial maxima. *Nat. Commun.*, 7(1), 10796, doi: 10.1038/ncomms10796, 2016.
- 658 Chao, S., Shaw, P., and Wang, J.: Wind relaxation as possible cause of the South China Sea Warm Current. *J. Oceanogr.*,  
659 51(1), 111-132, doi: 10.1007/BF02235940, 1995.
- 660 Chen, C. A., and Huang, M.: A mid-depth front separating the South China Sea water and the Philippine sea water. *J. Oceanogr.*,  
661 52(1), 17-25, doi: 10.1007/BF02236530, 1996.
- 662 Cheng, H., Edwards, R. L., Sinha, A., Spötl, C., Yi, L., Chen, S., Kelly, M., Kathayat, G., Wang, X., Li, X., Kong, X., Wang,  
663 Y., Ning, Y., and Zhang, H.: The Asian monsoon over the past 640,000 years and ice age terminations. *Nature*, 534(7609),  
664 640-646, doi: 10.1038/nature18591, 2016.
- 665 Chen, Y., Huang, E., Schefuß, E., Mohtadi, M., Steinke, S., Liu, J., Martínez-Méndez, G., and Tian, J.: Wetland expansion on  
666 the continental shelf of the northern South China Sea during deglacial sea level rise. *Quat. Sci. Rev.*, 231, 106202, doi:  
667 10.1016/j.quascirev.2020.106202, 2020.
- 668 Cheng, L., Abraham, J., Hausfather, Z., and Trenberth, K. E.: How fast are the oceans warming? *Science*, 363(6423), 128-129,  
669 doi: 10.1126/science.aav7619, 2019.
- 670 Cheng, Z., Wu, J., Luo, C., Liu, Z., Huang, E., Zhao, H., Dai, L., and Weng, C.: Coexistence of savanna and rainforest on the  
671 ice-age Sunda Shelf revealed by pollen records from southern South China Sea. *Quat. Sci. Rev.*, 301, 107947, doi:  
672 10.1016/j.quascirev.2022.107947, 2023.
- 673 [Clark, P. U., Shakun, J. D., Baker, P. A., Bartlein, P. J., Brewer, S., Brook, E., Carlson, A. E., Cheng, H., Kaufman, D. S., Liu,](#)  
674 [Z., Marchitto, T. M., Mix, A. C., Morrill, C., Otto-Blietsner, B. L., Pahnke, K., Russell, J. M., Whitlock, C., Adkins, J. F.,](#)  
675 [Blois, J. L., Clark, J., Colman, S. M., Curry, W. B., Flower, B. P., He, F., Johnson, T. C., Lynch-Stieglitz, J., Markgraf,](#)  
676 [V., McManus, J., Mitrovica, J. X., Moreno, P. I., and Williams, J. W.: Global climate evolution during the last deglaciation.](#)  
677 [\*Proc. Natl. Acad. Sci. U. S. A.\*, 109\(19\), E1134-E1142, doi:10.1073/pnas.1116619109, 2012.](#)
- 678 Clift, P. D., Hodges, K. V., Heslop, D., Hannigan, R., Van Long, H., and Calves, G.: Correlation of Himalayan exhumation  
679 rates and Asian monsoon intensity. *Nat. Geosci.*, 1(12), 875-880, doi: 10.1038/ngeo351, 2008.
- 680 Conedera, M., Tinner, W., Neff, C., Meurer, M., Dickens, A. F., and Krebs, P.: Reconstructing past fire regimes: methods,  
681 applications, and relevance to fire management and conservation. *Quat. Sci. Rev.*, 28(5), 555-576, doi:  
682 10.1016/j.quascirev.2008.11.005, 2009.
- 683 Dai, L., and Weng, C.: A survey on pollen dispersal in the western Pacific Ocean and its paleoclimatological significance as a  
684 proxy for variation of the Asian winter monsoon. *Sci. China Earth Sci.*, 54(2), 249-258, doi: 10.1007/s11430-010-4027-  
685 7, 2011.
- 686 Dai, L., and Weng, C.: Marine palynological record for tropical climate variations since the late last glacial maximum in the  
687 northern South China Sea. *Deep-Sea. Res. Pt II*, 122, 153-162, doi: 10.1016/j.dsr2.2015.06.011, 2015.

688 Dai, L., Weng, C., and Mao, L.: Patterns of vegetation and climate change in the northern South China Sea during the last  
689 glaciation inferred from marine palynological records. *Palaeogeogr., Palaeoclimatol., Palaeoecol.*, 440, 249-258, doi:  
690 10.1016/j.palaeo.2015.08.041, 2015.

691 Dale, B.: Dinoflagellate cyst ecology: modeling and geological applications. In J. Jansoni and D. C. McGregor (Eds.),  
692 *Palynology: principles and applications* (Vol. 3, pp. 1249-1275). American Association of Stratigraphic Palynologists  
693 Foundation, 1996.

694 Ding, Z., Yu, Z., Rutter, N. W., and Liu, T.: Towards an orbital time scale for chinese loess deposits. *Quat. Sci. Rev.*, 13(1),  
695 39-70, doi: 10.1016/0277-3791(94)90124-4, 1994.

696 Fang, G., Fang, W. D., and Wang, K.: A survey of the study of the South China Sea upper ocean circulation. *Acta Oceanog.*  
697 *Tai.*, 37, 1-16, 1998.

698 Felden, J., Möller, L., Schindler, U., Huber, R., Schumacher, S., Koppe, R., Diepenbroek, M., and Glöckner, F. O.: PANGAEA  
699 – Data Publisher for Earth & Environmental Science. *Sci. Data*, 10(1), 347, doi: 10.1038/s41597-023-02269-x, 2023.

700 Govin, A., Holzwarth, U., Heslop, D., Ford Keeling, L., Zabel, M., Mulitza, S., Collins, J. A., and Chiessi, C. M.: Distribution  
701 of major elements in Atlantic surface sediments (36°N–49°S): Imprint of terrigenous input and continental weathering.  
702 *Geochem. Geophys. Geosyst.*, 13(1), doi: 10.1029/2011GC003785, 2012.

703 Grimm, E.: Tilia and TGView 19 version 2.0. 41. software. Springfield, USA: Illinois State Museum, Research and Collection  
704 Center, 2015.

705 Hanebuth, T., Statteger, K., and Grootes, P. M.: Rapid flooding of the Sunda Shelf: A late-glacial sea-level record. *Science*,  
706 288(5468), 1033-1035, doi: 10.1126/science.288.5468.1033, 2000.

707 Haynes, J. R.: *Foraminifera*. Palgrave Macmillan London, doi: 10.1007/978-1-349-05397-1, 1981.

708 Holzwarth, U., Esper, O., and Zonneveld, K.: Distribution of organic-walled dinoflagellate cysts in shelf surface sediments of  
709 the Benguela upwelling system in relationship to environmental conditions. *Mar. Micropaleontol.*, 64(1–2), 91-119, doi:  
710 10.1016/j.marmicro.2007.04.001, 2007.

711 Hu, D., Clift, P. D., Böning, P., Hannigan, R., Hillier, S., Blusztajn, J., Wan, S., and Fuller, D. Q.: Holocene evolution in  
712 weathering and erosion patterns in the Pearl River delta. *Geochem. Geophys. Geosyst.*, 14(7), 2349-2368, doi:  
713 10.1002/ggge.20166, 2013.

714 Hu, J., Kawamura, H., Hong, H., and Qi, Y.: A review on the currents in the South China Sea: Seasonal circulation, South  
715 China Sea warm current and Kuroshio intrusion. *J. Oceanogr.*, 56(6), 607-624, doi: 10.1023/A:1011117531252, 2000.

716 Huang, C., Wu, L., Cheng, J., Qu, X., Luo, Y., Zhang, H., Ye, F., and Wei, G.: Sedimentary responses to climatic variations  
717 and Kuroshio intrusion into the northern South China Sea since the last deglaciation. *Global Planet. Change*, 245, 104671,  
718 doi: 10.1016/j.gloplacha.2024.104671, 2025.

719 Huang, K., You, C., Lin, H., and Shieh, Y.: In situ calibration of Mg/Ca ratio in planktonic foraminiferal shell using time series  
720 sediment trap: A case study of intense dissolution artifact in the South China Sea. *Geochem. Geophys. Geosyst.*, 9(4),  
721 doi: 10.1029/2007GC001660, 2008.

722 Hughen, K. A., Baillie, M. G. L., Bard, E., Warren Beck, J., Bertrand, C. J. H., Blackwell, P. G., Buck, C. E., Burr, G. S.,  
723 Cutler, K. B., Damon, P. E., Edwards, R. L., Fairbanks, R. G., Friedrich, M., Guilderson, T. P., Kromer, B., McCormac,  
724 G., Manning, S., Bronk Ramsey, C., Reimer, P. J., Reimer, R. W., Remmele, S., Southon, J. R., Stuiver, M., Talamo, S.,  
725 Taylor, F. W., Van der Plicht, J., and Weyhenmeyer, C. E.: Marine04 marine radiocarbon age calibration, 0–26 cal kyr  
726 BP. *Radiocarbon*, 46(3), 1059-1086, doi: 10.1017/S0033822200033002, 2004.

727 Jiwaringrueangkul, T., and Liu, Z.: East Asian monsoon and sea-level controls on clay mineral variations in the southern  
728 South China Sea since the Last Glacial Maximum. *Quat. Int.*, 592, 1-11, doi: 10.1016/j.quaint.2021.04.033, 2021.

729 Kaars, S. v. d., Wang, X., Kershaw, P., Guichard, F., and Setiabudi, D. A.: A Late Quaternary palaeoecological record from  
730 the Banda Sea, Indonesia: patterns of vegetation, climate and biomass burning in Indonesia and northern Australia.  
731 *Palaeogeogr., Palaeoclimatol., Palaeoecol.*, 155(1), 135-153, doi: 10.1016/S0031-0182(99)00098-X, 2000.

732 Kissel, C., Laj, C., Jian, Z., Wang, P., Wandres, C., and Rebolledo-Vieyra, M.: Past environmental and circulation changes in  
733 the South China Sea: Input from the magnetic properties of deep-sea sediments. *Quat. Sci. Rev.*, 236, 106263, doi:  
734 10.1016/j.quascirev.2020.106263, 2020.

735 Lambeck, K., Rouby, H., Purcell, A., Sun, Y., and Sambridge, M.: Sea level and global ice volumes from the Last Glacial  
736 Maximum to the Holocene. *Proc. Natl. Acad. Sci. U. S. A.*, 111(43), 15296-15303, doi: 10.1073/pnas.1411762111, 2014.

737 Laskar, J., Robutel, P., Joutel, F., Gastineau, M., Correia, A. C. M., and Levrard, B.: A long-term numerical solution for the  
738 insolation quantities of the Earth. *Astronomy & Astrophysics*, 428, 261-285, doi: 10.1051/0004-6361:20041335, 2004.

739 Lee, C. M., van Geel, B., and Gosling, W. D.: On the use of spores of coprophilous fungi preserved in sediments to indicate  
740 past herbivore presence. *Quaternary*, 5(3), 30, doi: 10.3390/quat5030030, 2022.

741 Li, C., Li, Y., Zheng, Y., Yu, S., Tang, L., Li, B., and Cui, Q.: A high-resolution pollen record from East China reveals large  
742 climate variability near the Northgrippian-Meghalayan boundary (around 42 years ago) exerted societal influence.  
743 *Palaeogeogr., Palaeoclimatol., Palaeoecol.*, 512, 156-165, doi: 10.1016/j.palaeo.2018.07.031, 2018a.

744 Li, L., Wang, H., Luo, B., and He, J.: The characterizations and paleoceanographic significances of organic and inorganic  
745 carbon in northern South China Sea during past 40 ka. *Mar. Geol. & Qua. Geol.*, 28(6), 79-85, doi:  
746 10.3724/sp.J.1140.2008.06079, 2008.

747 Li, M., Ouyang, T., Tian, C., Zhu, Z., Peng, S., Tang, Z., Qiu, Y., Zhong, H., and Peng, X.: Sedimentary responses to the East  
748 Asian monsoon and sea level variations recorded in the northern South China Sea over the past 3 kyr. *J. Asian Earth Sci.*,  
749 171, 213-224, doi: 10.1016/j.jseas.2018.01.001, 2019.

750 Li, Z., Pospelova, V., Kawamura, H., Luo, C., Mertens, K. N., Hernández-Almeida, I., Yin, K., Wu, Y., Wu, H., and Xiang,  
751 R.: Dinoflagellate cyst distribution in surface sediments from the South China Sea in relation to hydrographic conditions  
752 and primary productivity. *Mar. Micropaleontol.*, 159, 101815, doi: 10.1016/j.marmicro.2019.101815, 2020.

753 Li, Z., Pospelova, V., Lin, H.-L., Liu, L., Song, B., and Gong, W.: Seasonal dinoflagellate cyst production and terrestrial  
754 palynomorph deposition in the East Asian Monsoon influenced South China Sea: A sediment trap study from the  
755 Southwest Taiwan waters. *Rev. Palaeobot. Palynol.*, 257, 117-139, doi: 10.1016/j.revpalbo.2018.07.007, 2018b.

756 Li, Z., Pospelova, V., Liu, L., Francois, R., Wu, Y., Mertens, K. N., Saito, Y., Zhou, R., Song, B., and Xie, X.: High-resolution  
757 reconstructions of Holocene sea-surface conditions from dinoflagellate cyst assemblages in the northern South China Sea.  
758 *Mar. Geol.*, 438, 106528, doi: 10.1016/j.margeo.2021.106528, 2021.

759 Li, Z., Pospelova, V., Liu, L., Zhou, R., and Song, B.: High-resolution palynological record of Holocene climatic and  
760 oceanographic changes in the northern South China Sea. *Palaeogeogr., Palaeoclimatol., Palaeoecol.*, 483, 94-124, doi:  
761 10.1016/j.palaeo.2017.03.009, 2017.

762 Li, Z., Pospelova, V., Mertens, K. N., Liu, L., Wu, Y., Li, C., and Gu, H.: Evaluation of organic-walled dinoflagellate cyst  
763 distributions in coastal surface sediments of the China Seas in relation with hydrographic conditions for  
764 paleoceanographic reconstruction. *Quat. Int.*, 661, 60-75, doi: 10.1016/j.quaint.2023.03.007, 2023.

765 Lin, D., Chen, M., Yamamoto, M., and Yokoyama, Y.: Millennial-scale alkenone sea surface temperature changes in the  
766 northern South China Sea during the past 45,000 years (MD972146). *Quat. Int.*, 333, 207-215, doi:  
767 10.1016/j.quaint.2014.03.062, 2014.

768 Liu, J., Xiang, R., Chen, Z., Chen, M., Yan, W., Zhang, L., and Chen, H.: Sources, transport and deposition of surface  
769 sediments from the South China Sea. *Deep Sea Res. (I Oceanogr. Res. Pap.)*, 71, 92-102, doi: 10.1016/j.dsr.2012.09.006,  
770 2013.

771 Liu, J., Xiang, R., Kao, S. J., Fu, S., and Zhou, L.: Sedimentary responses to sea-level rise and Kuroshio Current intrusion  
772 since the Last Glacial Maximum: Grain size and clay mineral evidence from the northern South China Sea slope.  
773 *Palaeogeogr., Palaeoclimatol., Palaeoecol.*, 450, 111-121, doi: 10.1016/j.palaeo.2016.03.002, 2016a.

774 Liu, K., Chao, S., Shaw, P., Gong, G., Chen, C., and Tang, T.: Monsoon-forced chlorophyll distribution and primary production  
775 in the South China Sea: observations and a numerical study. *Deep Sea Res. (I Oceanogr. Res. Pap.)*, 49(8), 1387-1412,  
776 doi: 10.1016/S0967-0637(02)00035-3, 2002.

777 Liu, L., Guan, H., Feng, J., Xu, L., Mao, S., and Liu, L.: Composition of glycerol dibiphytanyl glycerol tetraethers (GDGTs)  
778 and its responses to paleotemperature and monsoon changes since 31ka in northern South China Sea. *Mar. Geol. & Qua.*  
779 *Geol.*, 40(3), 144-159, doi: 10.16562/j.cnki.0256-1492.2020021101, 2020.

780 Liu, Z., Colin, C., Li, X., Zhao, Y., Tuo, S., Chen, Z., Siringan, F. P., Liu, J. T., Huang, C.-Y., You, C.-F., and Huang, K.-F.:  
781 Clay mineral distribution in surface sediments of the northeastern South China Sea and surrounding fluvial drainage  
782 basins: Source and transport. *Mar. Geol.*, 277(1), 48-60, doi: 10.1016/j.margeo.2010.08.010, 2010.

783 Liu, Z., Trentesaux, A., Clemens, S. C., Colin, C., Wang, P., Huang, B., and Boulay, S.: Clay mineral assemblages in the  
784 northern South China Sea: implications for East Asian monsoon evolution over the past 2 million years. *Mar. Geol.*,  
785 201(1), 133-146, doi: 10.1016/S0025-3227(03)00213-5, 2003.

786 Liu, Z., Zhao, Y., Colin, C., Statterger, K., Wiesner, M. G., Huh, C., Zhang, Y., Li, X., Sompongchaiyakul, P., You, C., Huang,  
787 C., Liu, J. T., Siringan, F. P., Le, K. P., Sathiamurthy, E., Hantoro, W. S., Liu, J., Tuo, S., Zhao, S., Zhou, S., He, Z.,  
788 Wang, Y., Bunsomboonsakul, S., and Li, Y.: Source-to-sink transport processes of fluvial sediments in the South China  
789 Sea. *Earth-Sci. Rev.*, 153, 238-273, doi: 10.1016/j.earscirev.2015.08.005, 2016b.

790 Luo, C., Chen, C., Xiang, R., Jiang, W., Liu, J., Lu, J., Su, X., Zhang, Q., Yang, Y., and Yang, M.: Study of modern pollen  
791 distribution in the northeastern Indian Ocean and their application to paleoenvironment reconstruction. *Rev. Palaeobot.*  
792 *Palynol.*, 256, 50-62, doi: 10.1016/j.revpalbo.2018.05.007, 2018.

793 Luo, C., Chen, M., Xiang, R., Liu, J., Zhang, L., and Lu, J.: Comparison of modern pollen distribution between the northern  
794 and southern parts of the South China Sea. *Int. J. Biometeorol.*, 59(4), 397-415, doi: 10.1007/s00484-014-0852-2, 2015.

795 Luo, C., Jiang, C., Yang, M., Chen, M., Xiang, R., Zhang, L., Liu, J., and Pan, A.: Transportation modes of pollen in surface  
796 waters in the South China Sea and their environmental significance. *Rev. Palaeobot. Palynol.*, 225, 95-105, doi:  
797 10.1016/j.revpalbo.2015.11.004, 2016.

798 Luo, Y., and Sun, X.: Vegetation evolution and millennial-scale climatic fluctuations since Last Glacial Maximum in pollen  
799 record from northern South China Sea. *Chin. Sci. Bull.*, 50(8), 793-799, doi: 10.1007/BF03183681, 2005.

800 Luo, Y., and Sun, X.: Vegetation evolution and its response to climatic change during 3.15–0.67 Ma in deep-sea pollen record  
801 from northern South China Sea. *Chin. Sci. Bull.*, 58(3), 364-372, doi: 10.1007/s11434-012-5374-x, 2013.

802 [Maher, L.J.: Nomograms for computing 0.95 confidence limits of pollen data. \*Rev. Palaeobot. Palynol.\*, 13, 85-93, doi:  
803 10.1016/0034-6667\(72\)90038-3, 1972.](#)

804 Marret, F., and Zonneveld, K. A. F.: Atlas of modern organic-walled dinoflagellate cyst distribution. *Rev. Palaeobot. Palynol.*,  
805 125(1–2), 1-200, doi: 10.1016/S0034-6667(02)00229-4, 2003.

806 Matsuoka, K.: Dinoflagellate cysts and pollen in pelagic sediments of the northern part of the Philippin Sea. *Bull., Faculty of*  
807 *Liberal Arts, Nagasaki University. (Natural Science)*, 21(2), 59-70, 1981.

808 [Meyers, P.A.: Organic geochemical proxies of paleoceanographic, paleolimnologic, and paleoclimatic processes. \*Org.\*  
809 \*Geochem.\*, 27, 213-250, doi: 10.1016/S0146-6380\(97\)00049-1, 1997.](#)

810 Milliman, J. D., and Syvitski, J. P. M.: Geomorphic/tectonic control of sediment discharge to the ocean: The importance of  
811 small mountainous rivers. *J. Geol.*, 100(5), 525-544, doi: 10.1086/629606, 1992.

812 Mooney, S. D., and Tinner, W.: The analysis of charcoal in peat and organic sediments. *Mires Peat*, 7(09), doi:  
813 10.19189/001c.128417, 2011.

814 Oppo, D. W., and Sun, Y.: Amplitude and timing of sea-surface temperature change in the northern South China Sea: Dynamic  
815 link to the East Asian monsoon. *Geology*, 33(10), 785-788, doi: 10.1130/G21867.1, 2005.

816 Schönfeld, J., Alve, E., Geslin, E., Jorissen, F., Korsun, S., and Spezzaferri, S.: The FOBIMO (FORaminiferal Bio-MOnitoring)  
817 initiative—Towards a standardised protocol for soft-bottom benthic foraminiferal monitoring studies. *Mar.*  
818 *Micropaleontol.*, 94-95, 1-13, doi: 10.1016/j.marmicro.2012.06.001, 2012.

819 Smayda, T. J., and Trainer, V. L.: Dinoflagellate blooms in upwelling systems: Seeding, variability, and contrasts with diatom  
820 bloom behaviour. *Prog. Oceanogr.*, 85(1), 92-107, doi: 10.1016/j.pocean.2010.02.006, 2010.

821 Stibig, H.-J., Belward, A. S., Roy, P. S., Rosalina-Wasrin, U., Agrawal, S., Joshi, P. K., Beuchle, R., Fritz, S., Mubareka, S.,  
822 and Giri, C.: A land-cover map for South and Southeast Asia derived from SPOT-VEGETATION data. *J. Biogeogr.*,  
823 34(4), 625-637, doi: 10.1111/j.1365-2699.2006.01637.x, 2007.

824 Stuiver, M., and Reimer, P. J.: Extended 14C Data Base and Revised CALIB 3.0 14C Age Calibration Program. *Radiocarbon*,  
825 35(1), 215-230, doi: 10.1017/S0033822200013904, 1993.

826 Sun, X., Li, X., and Beug, H.-J.: Pollen distribution in hemipelagic surface sediments of the South China Sea and its relation  
827 to modern vegetation distribution. *Mar. Geol.*, 156(1), 211-226, doi: 10.1016/S0025-3227(98)00180-7, 1999.

828 Sun, X., Li, X., and Chen, H.: Evidence for natural fire and climate history since 37 ka BP in the northern part of the South  
829 China Sea. *Sci. China Ser. D-Earth Sci.*, 43(5), 487-493, doi: 10.1007/bf02875310, 2000a.

830 Sun, X., Li, X., Luo, Y., and Chen, X.: The vegetation and climate at the last glaciation on the emerged continental shelf of  
831 the South China Sea. *Palaeogeogr., Palaeoclimatol., Palaeoecol.*, 160(3), 301-316, doi: 10.1016/S0031-0182(00)00078-  
832 X, 2000b.

833 Sun, X., and Luo, Y.: Pollen record of the last 280 ka from deep sea sediments of the northern South China Sea. *Sci. China*  
834 *Ser. D-Earth Sci.*, 44(10), 879-888, doi: 10.1007/BF02907079, 2001.

835 Sun, X., Luo, Y., Huang, F., Tian, J., and Wang, P.: Deep-sea pollen from the South China Sea: Pleistocene indicators of East  
836 Asian monsoon. *Mar. Geol.*, 201(1), 97-118, doi: 10.1016/S0025-3227(03)00211-1, 2003.

837 Tang, L., Mao, L., Shu, J., Li, C., Shen, C., and Zhou, Z.: Atlas of Quaternary pollen and spores in China. Science Press and  
838 Springer Nature Singapore Pte Ltd, doi: 10.1007/978-981-13-7103-5, 2020.

839 ter Braak, C. J. F., and Smilauer, P.: Canoco reference manual and user's guide: software for ordination, version 5.0.  
840 Microcomputer Power, Ithaca, NY, USA. 2012.

841 Tian, J., Huang, E., and Pak, D. K.: East Asian winter monsoon variability over the last glacial cycle: Insights from a latitudinal  
842 sea-surface temperature gradient across the South China Sea. *Palaeogeogr., Palaeoclimatol., Palaeoecol.*, 292(1-2), 319-  
843 324, doi: 10.1016/j.palaeo.2010.04.005, 2010.

844 Tian, J., Wang, P. X., and Cheng, X. R.: Responses of foraminiferal isotopic variations at ODP Site 1143 in the southern South  
845 China Sea to orbital forcing. *Sci. China Ser. D-Earth Sci.*, 47(10), 943-953, doi: 10.1360/03yd0129, 2004.

846 Tian, J., Xie, X., Ma, W., Jin, H., and Wang, P.: X-ray fluorescence core scanning records of chemical weathering and monsoon  
847 evolution over the past 5 Myr in the southern South China Sea. *Paleoceanography*, 26(4), doi: 10.1029/2010PA002045,  
848 2011.

849 Tyszkla, J., Godos, K., Goleń, J., and Radmacher, W.: Foraminiferal organic linings: Functional and phylogenetic challenges.  
850 *Earth-Sci. Rev.*, 220, 103726, doi: 10.1016/j.earscirev.2021.103726, 2021.

851 Wan, S., and Jian, Z.: Deep water exchanges between the South China Sea and the Pacific since the last glacial period.  
852 *Paleoceanography*, 29(12), 1162-1178, doi: 10.1002/2013PA002578, 2014.

853 Wan, S., Li, A., Clift, P. D., and Stuut, J.-B. W.: Development of the East Asian monsoon: Mineralogical and sedimentologic  
854 records in the northern South China Sea since 20 Ma. *Palaeogeogr., Palaeoclimatol., Palaeoecol.*, 254(3), 561-582, doi:  
855 10.1016/j.palaeo.2007.07.009, 2007.

856 Wang, C.: The forests of China. Maria Moors Cabot Foundation No.5. Harvard University, Cambridge Mass, USA, 717, 1961.

857 Wang, L., Sarnthein, M., Erlenkeuser, H., Grootes, P. M., Grimalt, J. O., Pelejero, C., and Linck, G.: Holocene variations in  
858 Asian monsoon moisture: A bi-decadal sediment record from the South China Sea. *Geophys. Res. Lett.*, 26(18), 2889-  
859 2892, doi: 10.1029/1999GL900443, 1999.

860 Wang, P., Li, Q., and Tian, J.: Pleistocene paleoceanography of the South China Sea: Progress over the past 20years. *Mar.*  
861 *Geol.*, 352, 381-396, doi: 10.1016/j.margeo.2014.03.003, 2014.

862 Wang, P., and Sun, X.: Last glacial maximum in China: comparison between land and sea. *Catena*, 23(3), 341-353, doi:  
863 10.1016/0341-8162(94)90077-9, 1994.

864 Wang, P., Wang, B., Cheng, H., Fasullo, J., Guo, Z., Kiefer, T., and Liu, Z.: The global monsoon across time scales:  
865 Mechanisms and outstanding issues. *Earth-Sci. Rev.*, 174, 84-121, doi: 10.1016/j.earscirev.2017.07.006, 2017.

866 Wang, X., Sun, X., Wang, P., and Stattegger, K.: Vegetation on the Sunda Shelf, South China Sea, during the Last Glacial  
867 Maximum. *Palaeogeogr., Palaeoclimatol., Palaeoecol.*, 278(1), 88-97, doi: 10.1016/j.palaeo.2009.04.008, 2009.

868 Wang, Y. J., Cheng, H., Edwards, R. L., An, Z. S., Wu, J. Y., Shen, C.-C., and Dorale, J. A.: A high-resolution absolute-dated  
869 late Pleistocene monsoon record from Hulu Cave, China. *Science*, 294(5550), 2345-2348, doi: 10.1126/science.1064618,  
870 2001.

871 Wei, G., Liu, Y., Li, X., Shao, L., and Fang, D.: Major and trace element variations of the sediments at ODP Site 1144, South  
872 China Sea, during the last 230 ka and their paleoclimate implications. *Palaeogeogr., Palaeoclimatol., Palaeoecol.*, 212(3),  
873 331-342, doi: 10.1016/j.palaeo.2004.06.011, 2004.

874 Whitmore, T. C.: Rain forests: Tropical rain forests of the far east. *Science*, 228(4701), 874-875, doi:  
875 10.1126/science.228.4701.874, 1985.

876 Williams, G., Fensome, R., and MacRae, R.: DINOFLAJ3, 2017.

877 Xie, S.-P., Deser, C., Vecchi, G. A., Ma, J., Teng, H., and Wittenberg, A. T.: Global Warming Pattern Formation: Sea Surface  
878 Temperature and Rainfall. *J. Clim.*, 23(4), 966-986, doi: 10.1175/2009JCLI3329.1, 2010.

879 Xie, X., Zheng, H.-B., and Qiao, P.-J.: Millennial climate changes since MIS 3 revealed by element records in deep-sea  
880 sediments from northern South China Sea. *Chin. Sci. Bull.*, 59(8), 776-784, doi: 10.1007/s11434-014-0117-9, 2014.

881 [Xu, D., Lu, H., Wu, N., Liu, Z., Li, T., Shen, C., and Wang, L.: Asynchronous marine-terrestrial signals of the last deglacial  
882 warming in East Asia associated with low- and high-latitude climate changes. \*Proc. Natl. Acad. Sci. USA\*, 110, 9657-  
883 9662, 10.1073/pnas.1300025110, 2013.](#)

884 Yu, S., Zheng, Z., Chen, F., Jing, X., Kershaw, P., Moss, P., Peng, X., Zhang, X., Chen, C., Zhou, Y., Huang, K., and Gan, H. :  
885 A last glacial and deglacial pollen record from the northern South China Sea: New insight into coastal-shelf  
886 paleoenvironment. *Quat. Sci. Rev.*, 157, 114-128, doi: 10.1016/j.quascirev.2016.12.012, 2017.

887 Yuan, D., Cheng, H., Edwards, R. L., Dykoski, C. A., Kelly, M. J., Zhang, M., Qing, J., Lin, Y., Wang, Y., Wu, J., Dorale, J.,  
888 A., An, Z., and Cai, Y.: Timing, duration, and transitions of the last interglacial asian monsoon. *Science*, 304(5670), 575-  
889 578, doi: 10.1126/science.1091220, 2004a.

890 Yuan, Y. C., Bu, X. W., Liao, G. H., Lou, R. Y., Su, J. L., and Wang, K. S.: Diagnostic calculation of the upper-layer circulation  
891 in the South China Sea during the winter of 1998. *Acta Oceanol. Sin.*, 23(2), 187-199, 2004b.

892 Zhang, H., Liu, C., Jin, X., Shi, J., Zhao, S., and Jian, Z.: Dynamics of primary productivity in the northern South China Sea  
893 over the past 24,000 years. *Geochem. Geophys. Geosyst.*, 17(12), 4878-4891, doi: 10.1002/2016GC006602, 2016.

894 Zhao, X., Dupont, L., Schefuß, E., Bouimetarhan, I., and Wefer, G.: Palynological evidence for Holocene climatic and  
895 oceanographic changes off western South Africa. *Quat. Sci. Rev.*, 165, 88-101, doi: 10.1016/j.quascirev.2017.04.022,  
896 2017.

897 Zheng, Z., and Lei, Z. Q.: A 400,000 year record of vegetational and climatic changes from a volcanic basin, Leizhou Peninsula,  
898 southern China. *Palaeogeogr., Palaeoclimatol., Palaeoecol.*, 145(4), 339-362, doi: 10.1016/S0031-0182(98)00107-2,  
899 1999.

900 Zhong, Y., Chen, Z., Li, L., Liu, J., Li, G., Zheng, X., Wang, S., and Mo, A.: Bottom water hydrodynamic provinces and  
901 transport patterns of the northern South China Sea: Evidence from grain size of the terrigenous sediments. *Cont. Shelf*  
902 *Res.*, 140, 11-26, doi: 10.1016/j.csr.2017.01.023, 2017.

903 Zhou, B., Zheng, H., Yang, W., Taylor, D., Lu, Y., Wei, G., Li, L., and Wang, H.: Climate and vegetation variations since the  
904 LGM recorded by biomarkers from a sediment core in the northern South China Sea. *J. Quat. Sci.*, 27(9), 948-955, doi:  
905 10.1002/jqs.2588, 2012.

906 Zonneveld, K. A. F., Harper, K., Klügel, A., Chen, L., De Lange, G., and Versteegh, G. J. M.: Climate change, society, and  
907 pandemic disease in Roman Italy between 200 BCE and 600 CE. *Sci. Adv.*, 10(4), eadk1033, doi: 10.1126/sciadv.adk1033,  
908 2024.

909 Zonneveld, K. A. F., Marret, F., Versteegh, G. J. M., Bogus, K., Bonnet, S., Bouimetarhan, I., Crouch, E., de Vernal, A.,  
910 Elshanawany, R., Edwards, L., Esper, O., Forke, S., Grosfjeld, K., Henry, M., Holzwarth, U., Kieft, J. F., Kim, S.,  
911 Ladouceur, S., Ledu, D., Chen, L., Limoges, A., Londeix, L., Lu, S. H., Mahmoud, M. S., Marino, G., Matsouka, K.,  
912 Matthiessen, J., Mildenhall, D. C., Mudie, P., Neil, H. L., Pospelova, V., Qi, Y., Radi, T., Richerol, T., Rochon, A.,  
913 Sangiorgi, F., Solignac, S., Turon, J. L., Verleye, T., Wang, Y., Wang, Z., and Young, M.: Atlas of modern dinoflagellate  
914 cyst distribution based on 2405 data points. *Rev. Palaeobot. Palynol.*, 191(0), 1-197, doi: 10.1016/j.revpalbo.2012.08.003,  
915 2013.

916 Zonneveld, K. A. F., and Pospelova, V.: A determination key for modern dinoflagellate cysts. *Palynology*, 39(3), 387-409, doi:  
917 10.1080/01916122.2014.990115, 2015.

918 Zonneveld, K. A. F., Versteegh, G., and Kodrans-Nsiah, M.: Preservation and organic chemistry of Late Cenozoic organic-  
919 walled dinoflagellate cysts: A review. *Mar. Micropaleontol.*, 68(1-2), 179-197, doi: 10.1016/j.marmicro.2008.01.015,  
920 2008.